

EFFECT OF OXIDATIVE WEATHERING ON *IN VITRO*  
BIOACCESSIBILITY OF TOXIC SUBSTANCES IN  
CONTAMINATED, MINE TAILINGS-BORNE DUSTS

by

Andrew Thomas

---

Copyright © Andrew Thomas, 2016

A Thesis Submitted to the Faculty of the  
DEPARTMENT OF SOIL, WATER AND ENVIRONMENTAL SCIENCE

In Partial Fulfillment of the Requirements

For the Degree of

MASTER OF SCIENCE

In the Graduate College

THE UNIVERSITY OF ARIZONA

2016

STATEMENT BY AUTHOR

The thesis titled *Effect of Oxidative Weathering on In Vitro Bioaccessibility of Toxic Substances in Contaminated, Mine Tailings-Borne Dusts* prepared by Andrew Thomas has been submitted in partial fulfillment of requirements for a master's degree at the University of Arizona and is deposited in the University Library to be made available to borrowers under rules of the Library.

Brief quotations from this thesis are allowable without special permission, provided that an accurate acknowledgement of the source is made. Requests for permission for extended quotation from or reproduction of this manuscript in whole or in part may be granted by the head of the major department or the Dean of the Graduate College when in his or her judgment the proposed use of the material is in the interests of scholarship. In all other instances, however, permission must be obtained from the author.

SIGNED: *Andrew Thomas*

APPROVAL BY THESIS DIRECTOR

This thesis has been approved on the date shown below:

---

*Jon Chorover*

*Department Head, Soil, Water and Environmental Science*

*Defense date*

*6/28/2016*

## ACKNOWLEDGEMENTS

I would like to thank my advisor Dr. Jon Chorover, and Robert Root and Craig Rasmussen, the other members of my defense committee, for their support and encouragement throughout this project. This project would not have been possible without the assistance and encouragement of Dr. Chorover and Dr. Root.

In addition, I would like to acknowledge and thank the other members of the Environmental Geochemistry group and the Arizona Laboratory for Emerging Contaminants for their assistance with this project. I would especially like to thank Mary Kay Amistadi for her contributions to the project. Avelino Eduardo Sáez of the University of Arizona's Department of Chemical and Environmental Engineering granted access to a dust generator necessary for this project. Portions of this research were also carried out at the Stanford Synchrotron Radiation Lightsource in Palo Alto, CA, I would like to thank SSRL for granting access as well as the facility's staff for providing assistance. Additionally, I would like to thank Paul Wallace of the University of Arizona's University Spectroscopy and Imaging Facilities for his assistance with the SEM imaging portion of this project and Scott White for his assistance with sample collection.

## TABLE OF CONTENTS

ABSTRACT.....	5
CHAPTER I-INTRODUCTION.....	7
APPENDIX A: Oxidative weathering alters trace element bioaccessibility in PM <sub>10</sub> emissions from sulfide mine tailings.....	21
REFERENCES.....	74

## Abstract

Due to the history of hardrock mining in the southwestern United States, environmental contamination at legacy mine sites is an ongoing problem. Mine wastes, the primary source of contamination, particularly tailings are the uneconomical byproducts of hardrock mining that are generally deposited near a mine. Due to the geochemistry of sulfide orebodies (the source of many valuable metals including Zn, Pb, and Cu), the residues of sulfide ore extraction often have high concentrations of toxic contaminants such as As, Pb and Cd, which are released into the environment due to chemical and mineralogical changes following exposure of the tailings to oxygen and water. The secondary precipitates formed by tailings oxidation are primarily fine particles and due to the dry climate of desert southwestern US, the lack of soil moisture and structure, and the lack of vegetative cover on the tailings surface, contaminated dusts consisting of these secondary precipitates can be generated and spread to nearby communities by wind erosion of the tailings surface. Ingestion or inhalation of these wind-borne dusts can cause health problems resulting from contaminant exposure that depend on the lability of the contaminants in the biofluids that the dust particles come into contact with, a parameter that can be determined using *in vitro* bioaccessibility assays.

This research project concentrated on a tailings pile at the Iron King Mine and Humboldt Smelter Superfund site (IKMHSSS), a disused mine site located in the town of Dewey-Humboldt, AZ. Previous studies at IKHMSSS have revealed that the top meter of the tailings pile encompasses the entirety of a general pyrite ( $\text{FeS}_2$ ) weathering

sequence, with the lower levels dominated by pyrite and other minor sulfide minerals (e.g. ZnS, FeAsS, PbS), an intermediate layer dominated by sulfate salts, ferrihydrite and other amorphous Fe(III) oxyhydroxides, and a surface layer dominated by crystalline tertiary precipitates such as jarosite ( $\text{KFe}_3(\text{SO}_4)_2(\text{OH})_6$ ). Samples were taken from seven distinct layers differentiated by color, texture and morphological characteristics, and the  $\text{PM}_{10}$  fraction of each sample was isolated using a cyclone dust generator. The  $\text{PM}_{10}$  samples were then treated with synthetic biofluids designed to mimic physiological conditions present in the human respiratory system and gastrointestinal tract, and the aqueous concentrations of As, Fe, Pb and  $\text{SO}_4$  were measured at successive time points to determine the chemical kinetics of contaminant release into the synthetic interstitial fluids. The solution data was complemented by x-ray diffraction and x-ray absorption spectroscopy experiments performed at the Stanford Synchrotron Radiation Laboratory. These studies found that the *in vitro* bioaccessibility of both Pb and As was highest for the unweathered deep tailings samples and lowest for the partially-oxidized transition zone samples. The primary factors found to control bioaccessibility were the presence of labile  $\text{Fe}^{3+}$  and  $\text{SO}_4^{2-}$  in the samples, both of which are required to drive the precipitation of secondary minerals capable of incorporating trace elements such as As and Pb into their structure.

# Chapter 1: Introduction

## *1. Sulfide Mine Tailings*

Tailings are the uneconomical byproducts of sulfide ore extraction and are typically deposited on a pile at the surface (Wills, 2006). Volcanogenic massive sulfide orebodies, which constitute the majority of sulfide ore deposits, typically consist of grains of useful ores such as galena (PbS), sphalerite (ZnS), molybdenite (MoS<sub>2</sub>), and chalcopyrite (CuFeS<sub>2</sub>) surrounded by gangue material (Galley et al., 2007), which is dominated by minerals such as quartz and pyrite (FeS<sub>2</sub>). Following extraction of ore from the sulfide orebody, grinding and crushing of the extracted material liberates the useful ore grains from the quartz and pyrite matrix (Wills, 2006). Flotation processes are then used to separate the ore from gangue particles based on detergent affinities for sulfide particle surfaces. After the ore particles are removed from the mixture for processing, the remaining gangue material is then deposited on a tailings pile. Because toxic metal (oids) such as As, Pb, Zn, Cd, and Cr are often associated with sulfide ore deposits (Misra, 2012), mine tailings derived from these deposits can cause contamination of the surrounding environment when exposed to the surface.

Because hardrock mining of sulfide ores has occurred since antiquity, tailings are a ubiquitous and persistent source of environmental contamination, particularly in areas with a long history of mining. In 1980, the Global 2000 report (Barney, 1980) predicted that from 1976 to 2000, 6 million acres (0.2% of the earth's surface) would be directly disturbed by mining operations. In the US, 38% of the total area disturbed by mining operations was utilized for disposal of mine wastes; this percentage varies by location

because surface-open-pit mining produces more waste than underground mining (Barney, 1980). The relative effects of waste deposits are also expected to increase in the future as high-grade resources are depleted and production shifts to low-grade ores, which produce more waste. The land area above does not include the surface disturbed by pre-1976 legacy sites or the surface indirectly affected by mining activities, which is unquantifiable. Included in the latter category are watersheds affected by erosion of waste deposits, acid mine drainage, and tailings dam failures. Dust spread from waste deposits can also contaminate soils in the surrounding area.

## ***2. Environmental Health Impacts of Mine Tailings***

Because toxic, chalcophilic metal (loid) contaminants such as As, Pb, Zn, Cd, and Hg are often associated with sulfide ore deposits, exposure to contaminated mine wastes is a major environmental health issue in mining-impacted communities. Contamination of water supplies (Concas et al., 2006) and particulate emissions from waste piles (Mendez & Maier, 2008) can impact human health in the affected areas.

### ***2.1 Acid Mine Drainage***

When exposed to surface conditions, sulfide minerals such as pyrite ( $\text{FeS}_2$ ) undergo oxidation, transforming the iron sulfide parent material into iron oxides and producing sulfuric acid, which acidifies the tailings and increases the lability of metallic contaminants (a more detailed description of this process can be found in Section 3). Although this process occurs naturally, mining accelerates it by: 1) transporting unweathered sulfides to the surface, and 2) crushing and grinding, which increases the surface area where oxidation can take place (Johnson, 2003). The potential for acid mine drainage generation depends on a variety of factors including precipitation, microbial

oxidation of pyrite and  $\text{Fe}^{2+}_{(\text{aq})}$ , carbonate minerals in the ore,  $\text{O}_2$  content of the gas and aqueous phases, and particularly the permeability of the tailings dump (Johnson & Hallberg, 2005). Water draining from mine waste dumps tends to be highly acidic and contain high concentrations of metal (loid) contaminants, potentially impacting local groundwater and surface water resources (Johnson & Hallberg, 2005).

## *2.2 Particulate Emissions*

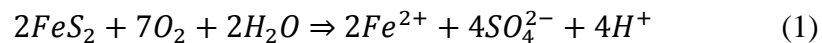
Due to sulfide oxidation processes, tailings surfaces are highly acidic and have high concentrations of toxic metal (loid) contaminants. As a result, phytotoxicity can prevent the growth of vegetative cover at the surface; these factors are related, as acidity increases the lability of metal cations (Mendez & Maier, 2008). The lack of vegetation at the surfaces of tailings piles can result in particulate dust emissions into nearby communities, an environmental impact that depends on climate (Mendez & Maier, 2008). In temperate, wet climates, contaminant leaching and acid mine drainage is the primary environmental impact of tailings piles; in contrast, particulate dust emissions have a stronger impact in (semi)arid regions such as the southwestern US and northwestern Mexico, where sulfide ore mining is an important part of the economy (Mendez & Maier, 2008). Particulate dust emissions have been found to be an important vector for contaminant transport into mining towns in this region including Nacozari, Sonora, Mexico (Meza-Figueroa et al., 2009) and Dewey-Humboldt, Arizona, USA (Stovern et al., 2016), where exposure to contaminated airborne dusts is a major environmental health concern.

## *2.3 Tailings Impoundment Failures*

Also known as tailings dams, impoundments are earth-fill embankment dams constructed in order to contain tailings and other mine wastes deposited behind them. Although designed to last permanently, tailings impoundments often fail, causing large-scale release of the impounded materials (Rico et al., 2008). In addition to the potential loss of life from landslides and flooding, tailings impoundment failures can also impact watersheds downstream with dissolved contaminants and contaminant-bearing particles. Recent major impoundment dam failures include the 2015 Bento Rodrigues dam failure, Brazil's largest ever environmental disaster, and the 2000 Baie Mare cyanide spill in Romania, which released about 100 metric tons of cyanide into the Danube River.

### 3. *The Pyrite Weathering Sequence*

Prior to oxidative weathering, sulfide mine tailings are a collection of fine-grained particles composed primarily of quartz and pyrite, with smaller amounts of carbonate and silicate minerals depending on the composition of the sulfide orebody. The addition of O<sub>2</sub> and H<sub>2</sub>O results in pyrite oxidation (Equation 1), releasing Fe<sup>2+</sup> and SO<sub>4</sub><sup>2-</sup> into the surrounding pore water (Nordstrom & Alpers, 1999).



Similar reactions occurring upon exposure of metal sulfide particles to oxidizing conditions result in the release of additional metal cations into solution. The high salinity and acidity resulting from these reactions accelerates oxidation (Blowes & Jambor, 1990; Blowes et al., 2003), eventually resulting in the precipitation of metastable secondary phases, including metal sulfate salts such as melanterite [FeSO<sub>4</sub>·7H<sub>2</sub>O], copiapite [Fe<sup>II</sup>Fe<sup>III</sup>(SO<sub>4</sub>)<sub>6</sub>(OH)<sub>2</sub>·22H<sub>2</sub>O], coquimbite [Fe<sub>2</sub>(SO<sub>4</sub>)<sub>3</sub>], gypsum (CaSO<sub>4</sub>·2H<sub>2</sub>O),

anglesite ( $\text{PbSO}_4$ ), and goslarite ( $\text{ZnSO}_4 \cdot 7\text{H}_2\text{O}$ ) (Jambor et al., 2000).  $\text{Fe}^{2+}_{(\text{aq})}$  oxidation to  $\text{Fe}^{3+}_{(\text{aq})}$  results in the precipitation via hydrolysis of short range-order Fe(III) oxyhydroxides and oxyhydroxysulfates such as ferrihydrite ( $\text{Fe}_2\text{O}_3 \cdot 0.5\text{H}_2\text{O}$ ) and schwertmannite [ $\text{Fe}_8\text{O}_8(\text{OH})_6(\text{SO}_4) \cdot n\text{H}_2\text{O}$ ] (Bigham & Nordstrom, 2000), the preferred hydrolysis product in acid sulfate waters in a pH-range of 2-4 (Bigham et al., 1996). These amorphous phases are metastable under acidic conditions (Bigham et al., 1996) and eventually transform to more crystalline Fe(III) oxyhydroxides and oxyhydroxysulfates such as goethite ( $\alpha\text{-FeOOH}$ ), hematite ( $\text{Fe}_2\text{O}_3$ ), and jarosite [ $\text{KFe}_3(\text{OH})_6(\text{SO}_4)_2$ ] (Schroth & Parnell, 2005; Acero et al., 2006; Wang et al., 2006).

In arid climates, oxidative sulfide tailings weathering follows a similar trajectory, but metastable sulfate salts and short range-order Fe(III) oxyhydroxides are more persistent due to the lack of pore water. Alternating periods of wetting and drying allow the repeated solvation and precipitation of efflorescent salts (mainly alkaline earth and metal sulfates) (Hudson-Edwards et al., 1999). In addition, the lack of water can prevent transformation of amorphous Fe(III) oxides to more crystalline phases such as jarosite. This transformation requires dissolution of the amorphous phase followed by precipitation of the crystalline phase, and dissolution is prevented by the lack of pore water. Previous studies of tailings in arid and semi-arid environments have shown persistence (Wray, 1998; Dold & Fontboté, 2001; Navarro et al., 2004, Hayes et al., 2009) of these metastable phases.

Previous studies (Hayes et al., 2014; Root et al., 2015) of oxidative weathering at the Iron King tailings surface have revealed the changes in mineralogy and elemental speciation associated with these weathering processes. A transect of the upper meter of

the tailings (Figure 1) was found to encompass the entirety of the pyrite weathering trajectory. An unweathered anoxic layer dominated by quartz, pyrite and carbonates is located at the bottom of the transect at a depth of approximately 70 cm. Above it is a sub-oxic, illuvial transition zone consisting primarily of pyrite and amorphous Fe(III) oxides, and a surface layer composed primarily of jarosite.

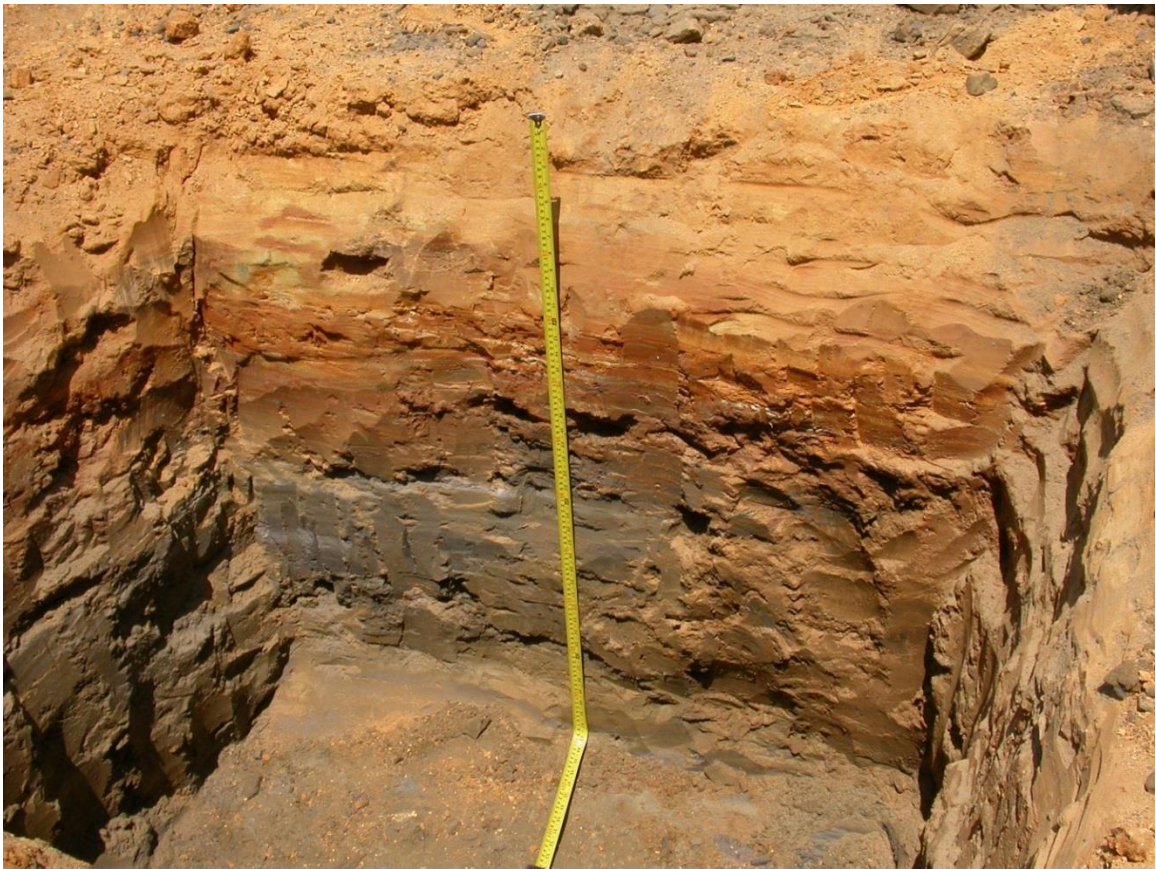


**Figure 1** Cross-section of the upper meter of the IKMHSS tailings profile.

Root et al. (2015) also investigated the speciation of trace elements (As, Pb, Zn) present in high concentrations across the tailings profile using x-ray absorption spectroscopy (XAS). This technique can be used to probe the molecular speciation and bonding environment of trace elements in tailings samples (Foster et al., 1998, Morin et al., 1999, Root et al., 2015). The results of these experiments (sections 4 and 5) and a

more detailed description of the technique (section 6) can be found elsewhere (Root et al., 2015).

#### ***4. Arsenic in Sulfide Mine Tailings***

When it is a constituent of a tailings deposit, arsenic is a major threat to human health due to its association with hyperkeratosis, diabetes, immunological diseases, bronchitis, and cardiac and renal diseases (Abernathy et al., 1999; Ahsan et al., 2006). For this reason and its abundance on the Earth's surface, arsenic is listed number one on the ATSDR (Agency for Toxic Substances and Disease Registry) priority list of hazardous contaminants (ATSDR, 2016). As a chalcophile, arsenic is often found associated with sulfide ore deposits, typically in the form of sulfide minerals such as arsenopyrite (FeAsS), orpiment (As<sub>2</sub>S<sub>3</sub>) and realgar ( $\alpha$ -As<sub>4</sub>S<sub>4</sub>) (Lengke et al., 2009; O'Day, 2006). Following transport to the surface and exposure to oxidizing conditions, the As in these minerals is transformed to arsenate (AsO<sub>4</sub><sup>3-</sup><sub>(aq)</sub>), which is released from the sulfide ore matrix and associates with various secondary weathering products (Foster et al., 1998).

Due to its high specific surface area and reactivity, ferrihydrite is known to have a high affinity for many trace element species (Davis & Kent, 1990), especially AsO<sub>4</sub><sup>3-</sup>, which is associated with ferrihydrite by adsorption and coprecipitation (Foster et al., 1998; Raven et al., 1998; Moldovan et al., 2003). AsO<sub>4</sub><sup>3-</sup><sub>(aq)</sub> binds to ferrihydrite by forming an inner-sphere, binuclear, bidentate complex that links the apical oxygens of adjacent Fe(III) oxyhydroxyl octahedra (Waychunas et al., 1993). By linking these octahedral complexes, AsO<sub>4</sub><sup>3-</sup> adsorption and coprecipitation has been found to inhibit ferrihydrite dissolution (Paige et al., 1997) by preventing the detachment and release of

Fe(III) from the ferrihydrite surface; as a result,  $\text{AsO}_4^{3-}$  on ferrihydrite is predicted to increase its persistence.

When ferrihydrite transforms to more crystalline phases in weathered sulfide mine tailings,  $\text{AsO}_4^{3-}(\text{aq})$  is released and often incorporated into the newly-formed crystalline precipitates. Isomorphic substitution of  $\text{AsO}_4^{3-}$  for  $\text{SO}_4^{2-}$  in the tetrahedral site of jarosite's structure has been observed and characterized (Paktunc & Dutrizac, 2003); if a divalent cation is available to balance the resulting change in structural charge, a complete solid solution series can be formed, including the end members beudantite  $[\text{PbFe}_3(\text{OH})_6\text{SO}_4\text{AsO}_4]$  and segnitite  $[\text{PbFe}_3(\text{AsO}_4)_2(\text{OH}, \text{H}_2\text{O})_6]$  (Dutrizac & Jambor, 2000). Adsorption and coprecipitation of  $\text{AsO}_4^{3-}$  with crystalline Fe(III) oxyhydroxides such as goethite and hematite is also possible (Waychunas et al., 1993; Fendorf et al., 1997; Catalano et al., 2007), although these phases have lower capacities for  $\text{AsO}_4^{3-}$  adsorption and coprecipitation than ferrihydrite (Dixit & Hering, 2003).

Root et al. (2015) investigated changes in arsenic speciation across the upper meter of the Iron King tailings pile, encompassing the entire sulfide weathering trajectory. Arsenic was found to originate as arsenopyrite ( $\text{FeAsS}$ ) in the unweathered tailings before coprecipitating with ferrihydrite in the amorphous ferric oxide-dominated transition layers. Because  $\text{AsO}_4^{3-}$  coprecipitated with ferrihydrite and jarosite could not be differentiated with the methods used, the arsenic speciation of the surface layers was not precisely determined using XAS, but speciation was possible through the use of selective sequential extractions.

##### ***5. Lead in Sulfide Mine Tailings***

Lead, a very common, highly persistent environmental contaminant, is often associated with sulfide orebodies and the tailings produced by the extraction of these deposits (Dudka & Adriano, 1997). Due primarily to its neurotoxic effects (Bressler & Goldstein, 1991), which are particularly hazardous in a neo-natal or pediatric context (Lidsky & Schneider, 2003), lead is listed number two on the ATSDR priority list of hazardous substances (ATSDR, 2016). In sulfide ore deposits, lead is usually present in the form of galena (PbS), but can also be present in the carbonate fraction (Ostergren et al., 1999) of calcareous tailings as cerussite (PbCO<sub>3</sub>). Following oxidation of galena, lead is released into solution as Pb<sup>2+</sup><sub>(aq)</sub>, which then concentrates in secondary precipitate phases (Hayes et al., 2009) such as anglesite (PbSO<sub>4</sub>), plumbojarosite [Pb<sub>0.5</sub>Fe<sub>3</sub>(SO<sub>4</sub>)<sub>2</sub>(OH)<sub>6</sub>], and the surfaces of metal oxides, particularly ferrihydrite (Ostergren et al., 1999; Morin et al., 1999). Extensive oxidative weathering and acidification of tailings leads to precipitation of Pb<sup>2+</sup><sub>(aq)</sub> with plumbojarosite; this was the dominant Pb-bearing phase observed in the Iron King surface tailings by Root et al. (2015).

#### ***6. Synchrotron-based X-Ray Absorption Spectroscopy***

X-ray absorption spectroscopy (XAS) is a technique used to probe the oxidation state and bonding environment of a selected element in a sample. The wavelength at which x-ray absorption (and fluorescence) reach a maximum is known as the edge; it gives information on the oxidation states of an element present in the sample (Bunker, 2010). Above the edge, a photoelectron “wave” emitted by the excited atom interferes with the incident beam and generates an interference pattern; this pattern gives information about the bonding environment of the analyzed element in the sample. In

order for this technique to work, a high-intensity, unidirectional, easily-tuned incident beam must be generated, which is made possible by the use of synchrotron radiation (Bunker, 2010).

Synchrotron radiation is so named because it is generated as a byproduct of synchrotron particle accelerators, which are cyclic accelerators that bring electrons to relativistic velocities by varying a magnetic field over time, adapting to the increasing relativistic mass of the accelerated particles (Kim, 1989). Booster synchrotrons accelerate the particle beam to the desired energy, after which the beam is “injected” into a storage ring. The particle beam in the storage ring circulates continuously; insertion devices such as bending magnets, wigglers and undulators along the beam’s pathway change its direction and therefore its velocity vector, generating a tangential x-ray beam (Kim, 1989). Bending magnets are constant dipole magnets inserted at points in the storage ring where the particle beam changes direction and generate a tangential x-ray beam due to changes in particle velocity (Winick et al., 1981). Although this method generates an x-ray beam of sufficient intensity and spectral range for spectroscopy experiments, it is designed to maintain a circulating beam, and other insertion devices are more effective at generating useful radiation (Winick, 1981). These insertion devices, which are installed along the straight portions of the storage ring, do not cause displacement of the particle beam but produce synchrotron radiation of much higher intensity than the radiation generated by bending magnets. Wigglers and undulators consist of alternating magnetic fields that deflect the beam in alternating directions, producing an angular excursion of the beam (Winick et al., 1981). Beams generated by these devices have higher intensities and wider spectral ranges than beams generated by bending magnets, making them more

useful for spectroscopy. Beamlines 4-3 and 11-2 at the Stanford Synchrotron Radiation Laboratory in Palo Alto, CA, which were used for all x-ray absorption spectroscopy experiments, both use wigglers as light sources.

X-ray absorption fine-structure (XAFS) spectroscopy is based on the principle of the photoelectric effect. When an incident photon of sufficient energy above the absorption edge reaches an atom in a sample, it is absorbed by an electron in an inner atomic orbital (e.g.  $1s$ ), which is then ejected from the atom (Konigsberger & Prins, 1988). At incident photon energies above the absorption edge, the ejected photoelectron has kinetic energy and behaves as a photoelectron “wave”, scattering off of the atoms surrounding the excited atom. This causes interferences between the scattered and incident waves that manifest as an interference pattern in the post-edge region of the transmission spectrum, which quantifies absorption as a function of wavelength (Konigsberger & Prins, 1988). The ejection of the electron leaves a core-hole in the vacated atomic orbital that is soon occupied by an electron from a higher-energy orbital, and the x-ray wavelength emitted by this quantized relaxation is also detected in order to generate a fluorescence spectrum with identical features.

After transformation of the raw data, XAS spectra can be used to determine elemental speciation and bonding environment through the use of reference spectra. If the raw data has sufficient resolution, a XANES (x-ray absorption near-edge spectroscopy) spectrum can be generated; by least-squares fitting of linear combinations of reference spectra to a sample spectrum, the relative components of the target element’s speciation can be determined (Konigsberger & Prins, 1988). Similarly, elemental speciation can be determined using linear combinations of post edge data converted to  $k$ -space (frequency

domain) following normalization of the post-edge region (Bunker, 1981). The XAS data collection and linear combination fitting program Athena (0.9.24, Ravel and Newville, 2005) determines a linear combination of weighted reference standard components that match the spectrum obtained from the sample; the relative weights of each component returned by Athena were reported for all XAS experiment results.

### **7. *In vitro* Bioaccessibility Assays**

Following ingestion or inhalation of airborne dusts near tailings sites, dust particles come into contact with fluids in the stomach (gastric fluid) and lungs (alveolar fluid). Because toxic contaminants are often present in insoluble phases and have low bioavailability, actual exposures to substances present in the inhaled and/or ingested materials are lower than the total contaminant concentrations present (Ruby et al. 1996, Rodriguez et al. 1999), complicating efforts at establishing dose-response relationships. *In vitro* bioaccessibility assays (IVBAs) are an effective, laboratory-based, low cost method of estimating the bioaccessibility of a contaminant in gastric or alveolar fluid, or the fraction of the contaminant released into the biofluid (Oomen et al., 2002). The bioaccessible fraction of a contaminant can then be used to predict the actual dose of contaminant and the resulting toxicological effects.

Prior to the use of IVBAs for studies of toxic contaminants, similar assays were used in nutrition studies to assess the bioavailability of iron from food (Miller et al., 1981). These multi-step assays were designed to mimic the physiological conditions and residence time of each step in the digestive system: the stomach, the small intestine, and the large intestine. Later, similar multi-step systems known as physiologically-based extraction tests (PBETs) were used to determine the bioavailability of toxic contaminants

such as arsenic and lead in contaminated soil samples (Ruby et al. 1996, Rodriguez et al. 1999, Beak et al., 2006). In these assays, the gastric fluid step played the most important role in determining *in vitro* bioaccessibility of contaminants because most As- and Pb-bearing phases are more soluble under acidic, low-O<sub>2</sub> conditions; in addition, Ruby et al. (1996;1999) found that bioaccessibility values determined from the gastric fluid digestion step correlated well with *in vivo* values observed in rats and pigs. For this reason, a simplified, one-step gastric fluid IVBA was designed by the Solubility/Bioavailability Research Consortium (SBRC, 2001) and predicted to adequately estimate the bioaccessible fraction of As and Pb in gastric fluid. These experiments used a modified version of the gastric IVBA protocol designed by the SBRC. Concentrated (12M) HCl was used to adjust the pH of a 0.4 M glycine solution to mimic normal, non-fasting conditions in the stomach, i.e. pH 1.5-1.8.

Inhalation exposure to toxic substances present in airborne dusts depends on the penetration of these dusts to what is termed the “deep lung”, or the alveoli located at the ends of the lung’s branching structure where gas exchange takes place (Sorokin & Brain, 1975). Here, the contaminated dust particles come into contact with alveolar fluid, where contaminants in the dust can be released and exchanged across the alveolar membrane into the bloodstream. Synthetic lung fluid attempts to mimic the chemical composition of alveolar fluid; the first attempt to do so was Gamble’s solution (Moss, 1979), which consisted of a mixture of inorganic and organic salts at concentrations approximating those estimated for actual alveolar fluid. Various other studies have modified this recipe by introducing new ingredients and modifying the concentrations of existing ones (Takaya et al., 2006; Taunton et al., 2010). Others modified the composition by adding

proteins such as albumin and mucin (Boisa et al., 2014), which comprise the mucus excreted by the lungs, and pulmonary surfactant (Stopford et al., 2003). For this experiment, a modified Gamble's solution used by Scholze and Conradt (1987), Takaya et al. (2006), and Menka et al. (2014) that included several additional organic acids and glycine was used.

#### **8. Present Study**

The present study aimed to determine the pharmacokinetic *in vitro* bioaccessible fractions of As and Pb that would release to synthetic biofluid at physiologically relevant time steps. Specifically, this study aimed to determine how the As and Pb bioaccessible fraction varied with mineralogical changes resulting from oxidative weathering of the sulfidic parent material, knowledge which can potentially allow the prediction of health risks resulting from mine waste sites at various stages of oxidation. To do so, a 1-meter deep pit was excavated at the surface of the IKMHSSS tailings pile and samples from distinct morphological horizons (Figure 1) were collected. After collection, the samples were air-dried and the PM<sub>10</sub> fractions collected using a rotating drum dust generator connected to a cyclone separator used for dust fractionation. The dust samples produced using this method were then treated with synthetic gastric and alveolar fluid, and As and Pb release from the dust samples was measured and used to quantify the bioaccessible fractions of these elements. XRD and XAS experiments were also performed on reacted and unreacted samples to relate bioaccessibility to changes in mineralogy and elemental speciation following sample treatment with synthetic biofluid.

Appendix A: Oxidative weathering alters trace element  
bioaccessibility in PM<sub>10</sub> emissions from sulfide mine tailings

Andrew N. Thomas, Robert A. Root, Mary Kay Amistadi, Jon Chorover\*

In preparation for submission to:

*Environmental Chemistry or Journal of Hazardous Materials*

\* Address correspondence to Jon Chorover, Department of Soil, Water and  
Environmental Science, University of Arizona, 1177 E 4<sup>th</sup> St, Shantz 429, Tucson, AZ  
85721 Telephone: +1 520-626-5635, Fax: 520-626-1647, E-mail:  
[chorover@email.arizona.edu](mailto:chorover@email.arizona.edu)

Andrew N. Thomas, Department of Soil, Water and Environmental Science, University  
of Arizona, 1177 E 4<sup>th</sup> St, Shantz 429, Tucson, AZ 85721 Telephone: +1 520-626-1566,  
Fax: 520-626-1647, E-mail: [andrewthomas@email.arizona.edu](mailto:andrewthomas@email.arizona.edu)

Robert Root, Department of Soil, Water and Environmental Science, University of  
Arizona, 1177 E 4<sup>th</sup> St, Shantz 429, Tucson, AZ 85721 Telephone: +1 520-626-5635,  
Fax: 520-626-1647, E-mail: [robroot.az@gmail.com](mailto:robroot.az@gmail.com)

Mary Kay Amistadi, Department of Soil, Water and Environmental Science, University of Arizona, 1177 E 4<sup>th</sup> St, Shantz 429, Tucson, AZ 85721 Telephone: +1 520-626-5635, Fax: 520-626-1647, E-mail: [ma@email.arizona.edu](mailto:ma@email.arizona.edu)

Jon Chorover, Department of Soil, Water and Environmental Science, University of Arizona, 1177 E 4<sup>th</sup> St, Shantz 429, Tucson, AZ 85721 Telephone: +1 520-626-5635, Fax: 520-626-1647, E-mail: [chorover@cals.arizona.edu](mailto:chorover@cals.arizona.edu)

## **Abstract**

Environmental contamination from mine waste deposits is a persistent problem in the western United States due to the long history of hard rock mining. Because of the geochemistry of sulfide ore deposits, they are often associated with toxic metal (loid)s such as As, Pb, Zn and Cd, which are released from the sulfide ore matrix by oxidative processes following exposure to O<sub>2</sub> and H<sub>2</sub>O at the surface and can potentially contaminate groundwater, surface water or soil in the surrounding area. In Dewey-Humboldt, AZ, the Iron King Mine and Humboldt Smelter Superfund (IKMHSS) site is composed of a tailings pile and disused smelter located in semi-arid central Arizona, USA. Ingestion or inhalation of contaminated fine particulate dust particles is a potential exposure route, as the dry climate, lack of soil structure and absence of vegetative cover allow the generation of toxic dust with the potential to impact the nearby community. *In vitro* bioaccessibility assays were used to determine the potential risk for trace element

release from dust ( $PM_{10} < 10 \mu\text{m}$  effective diameter) samples into simulated biofluids. Bioaccessibility assays have been applied to As and Pb in soils and mine tailings, but, to our knowledge, no study has attempted to link bioaccessibility to the chemical kinetics of trace element release and the dissolution and precipitation of associated mineral phases. In this study, tailings dust samples isolated from progressively increasing depths in the IK tailings pile were exposed to synthetic stomach and alveolar (lung) fluids. Aqueous concentrations of various elemental species were measured at selected time points to determine elemental release kinetics. X-ray diffraction and x-ray absorption spectroscopy experiments were performed to relate release kinetics to changes in solid phase mineralogy and elemental speciation. Results indicate that *in vitro* gastric and lung bioaccessibility was highest in unweathered tailings samples, while *in vitro* bioaccessibility was lowest in samples comprising a sub-oxic transition zone located at a depth of 40-52 cm. Several factors were found to control bioaccessibility in these samples, including the higher solubility of  $Fe^{2+}_{(aq)}$ , which dominates the mineralogy of the unweathered tailings, the presence of soluble  $SO_4^{2-}$ , which can drive precipitation of Fe(III) oxyhydroxysulfates such as jarosite, a major sink for Pb and As in this environment, and the presence of poorly-crystalline Fe(III) oxides such as ferrihydrite that are capable of adsorption of trace elements from solution. Ferrihydrite precipitation and incorporation of trace elements was also found to play a major role in controlling *in vitro* bioaccessibility.

# 1. INTRODUCTION

Tailings are the fine-grained, uneconomical byproducts of sulfide ore processing (crushing, grinding, froth flotation, etc.) that, following deposition on a tailings pile, can pose health risks to human populations nearby (Lottermoser, 2011). Because chalcophilic toxic contaminants (i.e. As, Pb, Zn, Cd) are often associated with sulfide ore bodies (Misra, 2012) that also contain valuable ores such as  $\text{CuFeS}_2$  (chalcopyrite), the exposure of sulfide ore material to oxygen and water results in oxidative dissolution of the sulfide tailings material (Boulet and Larocque, 1998) and release of contaminants to aqueous solution or secondary solid phases. These weathering processes can result in health risks to the surrounding populations if they result in generation of toxic dusts and transformation of contaminants to more labile forms.

## *1.1 Weathering Processes in Sulfide Tailings*

Following the initial exposure of the pyrite-rich mine wastes to oxygen and water at Earth's surface, oxidative dissolution of pyrite ( $\text{FeS}_2$ ) leads to the release of  $\text{SO}_4^{2-}$ ,  $\text{Fe}^{2+}$ , and protons ( $\text{H}^+$ ) to interstitial pore waters (Hayes et al., 2014). Trace elements, including  $\text{H}_2\text{AsO}_4^-$  (aq) and  $\text{Pb}^{2+}$  (aq), are released by oxidative dissolution of minor sulfide phases such as arsenopyrite ( $\text{FeAsS}$ ) and galena ( $\text{PbS}$ ) (Rimstidt et al., 1994; Basu and Schreiber, 2013), eventually leading to the formation of metastable secondary phases (Blowes and Jambor, 1990). Initially, this collection of secondary phases generally includes metal sulfates including melanterite [ $\text{FeSO}_4 \cdot 7\text{H}_2\text{O}$ ], copiapite [ $\text{Fe}^{\text{II}}\text{Fe}_4^{\text{III}}(\text{SO}_4)_6(\text{OH})_2 \cdot 22\text{H}_2\text{O}$ ], coquimbite [ $\text{Fe}_2(\text{SO}_4)_3$ ], gypsum ( $\text{CaSO}_4 \cdot 2\text{H}_2\text{O}$ ), anglesite ( $\text{PbSO}_4$ ), and goslarite ( $\text{ZnSO}_4 \cdot 7\text{H}_2\text{O}$ ) (Jambor et al., 2000). Further oxidation and acidification leads to

the formation of tertiary Fe (II) and Fe(III) oxyhydroxides and oxyhydroxysulfates such as goethite [ $\alpha$ -FeOOH], ferrihydrite [ $5\text{Fe}_2\text{O}_3 \cdot 9\text{H}_2\text{O}$ ], hematite [ $\text{Fe}_2\text{O}_3$ ], schwertmannite [ $\text{Fe}_8\text{O}_8(\text{OH})_6(\text{SO}_4) \cdot 10\text{H}_2\text{O}$ ], and jarosite [ $\text{KFe}_3(\text{SO}_4)_2(\text{OH})_6$ ] (Bigham et al., 1996; Bigham and Nordstrom, 2000). As the pH decreases due to sulfide oxidation, Fe(III) (hydr)oxides become increasingly unstable and oxyhydroxysulfates such as schwertmannite and jarosite become more prevalent (Bigham and Nordstrom, 2000). However, in the semi-arid environment found in central Arizona, wet-dry cycles and a lack of pore water throughflux facilitates the persistence of metastable minerals such as metal-sulfate salts and Fe oxyhydroxides that would normally be soluble under acidic conditions (Navarro et al., 2004; Meza-Figueroa et al., 2009). As tailings oxidation progresses, trace element species (especially  $\text{Pb}^{2+}_{(\text{aq})}$  and  $\text{H}_2\text{AsO}_4^{-}_{(\text{aq})}$ ) become associated with neo-formed secondary phases by adsorption and co-precipitation (Waychunas et al., 1993; Fuller et al., 1993; Raven et al., 1998; Savage et al., 2005; Root et al., 2015).

### *1.2 Arsenic in Sulfide Mine Tailings*

Because of its toxicity and its association with health problems such as hyperkeratosis, diabetes, immunological diseases, bronchitis, and cardiac and renal diseases (Abernathy et al., 1999; Ahsan et al., 2006), arsenic is recognized as a major threat to human health and is therefore listed number one on the ATSDR (Agency for Toxic Substances and Disease Registry) priority list of hazardous substances (ATSDR, 2016). When associated with sulfide mine tailings, arsenic typically originates in arsenic-bearing sulfides such as arsenopyrite ( $\text{FeAsS}$ ), orpiment ( $\text{As}_2\text{S}_3$ ), and realgar ( $\alpha$ - $\text{As}_4\text{S}_4$ ) associated with sulfide ore deposits (O'Day, 2006; Lengke et al., 2009). Extensive EXAFS studies of arsenic in sulfide mine tailings environments have found that arsenate

( $\text{AsO}_4^{3-}$ ) is the primary weathering product in the presence of sufficient oxygen and generally occurs in the form of the mineral scorodite ( $\text{FeAsO}_4$ ), poorly-crystalline ferric arsenates, a bidentate-binuclear inner-sphere adsorption complex on the surface of Fe(III) oxides, or  $\text{AsO}_4^{3-}$  coprecipitated with ferrihydrite or jarosite (Foster et al., 1998; Sherman and Randall, 2003; Paktunc et al., 2004; Root et al., 2015). Previous studies of the bioavailability of As in mine waste have suggested that oxidative weathering increases bioavailability because  $\text{AsO}_4^{3-}$  bearing phases are typically more soluble than the recalcitrant sulfide phases mentioned earlier (Craw & Bowell, 2014).

### *1.3 Lead in Sulfide Mine Tailings*

As a result of its persistence and relatively high concentration in the environment, lead is a major health concern associated with the weathered byproducts of sulfide mine tailings. Its primary detrimental effect on human health is its neurotoxicity (Bressler & Goldstein, 1991), which is particularly hazardous in a pediatric or pre-natal context (Lidsky & Schneider, 2003). Because of these effects, lead is number two on the ATSDR priority list of hazardous contaminants (ATSDR, 2016). In calcareous sulfide ore deposits like Iron King, lead is typically associated with the sulfide mineral galena ( $\text{PbS}$ ) as well as metal carbonates (Ostergren et al., 1999). Many studies (Ostergren et al., 1999; Morin et al., 1999; Hayes et al., 2009; Root et al., 2015) have shown that oxidative weathering redistributes  $\text{Pb}^{2+}_{(\text{aq})}$  into secondary weathering products such as cerussite ( $\text{PbCO}_3$ ), anglesite ( $\text{PbSO}_4$ ), plumbojarosite [ $\text{Pb}_{1/2}\text{Fe}_3(\text{SO}_4)_2(\text{OH})_6$ ], and the surfaces of amorphous metal oxide particles (particularly ferrihydrite). Similar studies have also shown that, in partially oxidized transition zones, lead mineralogy is dominated by Fe(III) oxide and sulfate phases that give way to plumbojarosite following oxidation and acidification

(Hayes et al., 2012). However, in semi-arid environments, there is evidence for persistence of metastable anglesite along with other metal sulfate salts (Meza-Figueroa et al., 2009; Hayes et al., 2012).

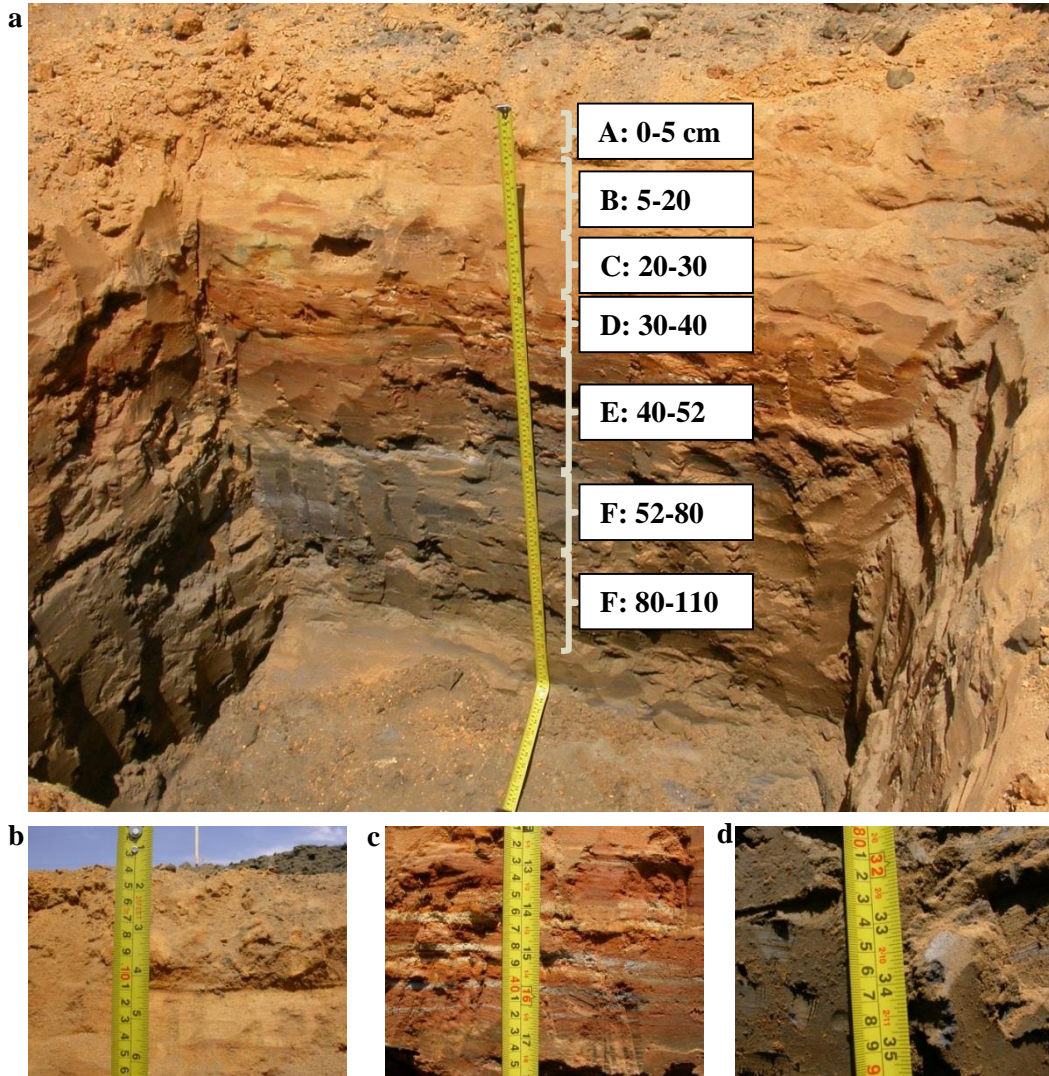


**Fig. 1** Cross-section of a sulfide tailings weathering sequence at the Iron King Superfund Site (Dewey-Humboldt, AZ). (a) Full transect of weathering profile, including sample delineations, (b) surface layers, (c) partially oxidized transition layers, (d) unweathered tailings parent material.

#### *1.4 Iron King Mine and Humboldt Smelter Superfund Site (IKMHSS) as a Model System*

Both arsenic and lead are present at highly elevated solid phase concentrations in the legacy IKMHSS site that has been the subject of ongoing study in our research group. We previously reported on the mineral weathering trajectory and related speciation changes of major (Fe, S) (Hayes et al., 2014) and trace elements (As, Pb, Zn) (Root et al., 2015) in the bulk fraction of the IKMHSS tailings by analyzing samples taken from the top two meters of the tailings pile. These samples were found to encompass the entirety of the general sulfide tailings weathering sequence from depth towards the tailings surface, including predominance of unweathered pyrite in the deepest zone, carbonates in the lower anoxic zone, a sub-oxic partially-oxidized transition zone dominated by pyrite and Fe(III) oxyhydroxides, and finally an oxidized zone at the surface primarily composed of Fe(III) oxyhydroxysulfates (Hayes et al. 2014). These mineralogical changes manifest as color variation that is visible to the naked eye when transitioning from anoxic to oxic conditions (Figure 1). The changes in mineralogy are also associated with important transitions in As, Pb, and Zn speciation. These trace elements were found to be concentrated in sulfide and carbonate phases in the anoxic zone before being redistributed to Fe oxide phases in the transition zone and jarosites and effervescent sulfate salts near the tailings surface (Root et al., 2015). Changes in mineralogy and trace element speciation affect the behavior of toxic contaminants after introduction into biological systems, as trace element release from tailings material when exposed to aqueous (including biological) fluids depends on the dissolution/precipitation and adsorption/desorption kinetics of associated mineral phases.

#### *1.5 Offsite Transport*

Because of the semi-arid climate of the area surrounding the IKHMSS, wind dispersion of dust particles is the primary means by which residents of the nearby community of Dewey-Humboldt, AZ are brought into contact with toxic metal (loid)s present in the tailings (Stovern et al., 2014). Because of the fine texture of the deposited tailings, the semi-arid climate of this area of central Arizona, and the lack of vegetative cover (due to the acidic pH and high toxicity of the surface), there is a high risk of particle detachment from the surface and transport into the nearby community, especially for the fine (clay and silt) particulate fraction ( $< 40 \mu\text{m}$ ), for which transport has been found to extend over regional scales (Csavina, et al. 2012). As a result, there are often significant dangers to human health in the case of inhalation or ingestion of contaminated particles (Moreno et al., 2007) or later exposure to contaminated soil, water or home garden crops following particle deposition (Ramirez-Andreotta, et al. 2013). When dust particles are ingested or inhaled, interactions between the particles and the interstitial fluids determine the possible health effects by mediating the amounts of toxic substances released after exposure (Kelley et al., 2002). In this study, the solubility of toxic contaminants such as As and Pb in gastric and lung fluid was determined via *in vitro* bioaccessibility assays, which were used to calculate the fraction of each metal released from the solid phase into solution.

### ***1.6 In vitro Bioaccessibility Assays***

Following inhalation or ingestion of airborne dust, dust particles come into contact with fluids in the lungs and gastrointestinal tract. Bioavailability studies have shown that actual exposures to toxic substances in ingested/inhaled materials may be significantly less than the total contaminant levels present (Ruby et al. 1996, Rodriguez et

al. 1999). The bioaccessibilities of toxic contaminants, or their solubilities in synthetic gastric or lung fluid, determine the effective doses of each substance, and therefore the toxicological effects.

Previous studies (Ruby et al. 1996, Rodriguez et al. 1999, Beak et al., 2006) have determined gastrointestinal bioaccessibility values for As and Pb in solid samples using multi-step assays known as physiologically-based extraction tests (PBETs); for this study, a one-step *in vitro* gastric bioaccessibility assay using a simplified synthetic gastric fluid composed of 0.4 M glycine acidified to a pH of 1.8 was performed. This procedure was adapted from a standard operating procedure developed by the Solubility/Bioavailability Research Consortium (SBRC). The synthetic lung fluid used was a modified Gamble's solution (Boisa et al. 2014) amended to include organic salts and amino acids (Scholze and Conradt 1987; Takaya et al. 2006; , Menka et al. 2014). When agitated continuously under physiological conditions, these synthetic biofluids mimic the conditions present at the particle-fluid interface following tailings ingestion or inhalation.

## **2. MATERIALS AND METHODS**

### ***2.1 Site Description***

The IKHMSS, located near Dewey-Humboldt, Arizona, USA, is a disused mine site that previously exploited a sulfide intrusive deposit located in a pre-Cambrian metamorphosed andesitic tuff within the Bradshaw Mountains (Creasey, 1952). Before the mine halted operations in 1969, large amounts [16,800 t Pb, 52,200 t Zn, 1,800 t Cu, 105 t Ag, and 3390 kg Au were produced from 1906 to 1947 (Hayes et al., 2014)] of

metals such as Cu, Zn, Pb, and small amounts of Au and Ag were extracted (Creasey, 1952), with the remaining wastes deposited as a tailings pile into a topographical depression located immediately east of the mine shaft (see Hayes et al., 2014 and Root et al., 2015 for site details). A total of approximately four million cubic meters of tailings were deposited at this site (Figure 2).

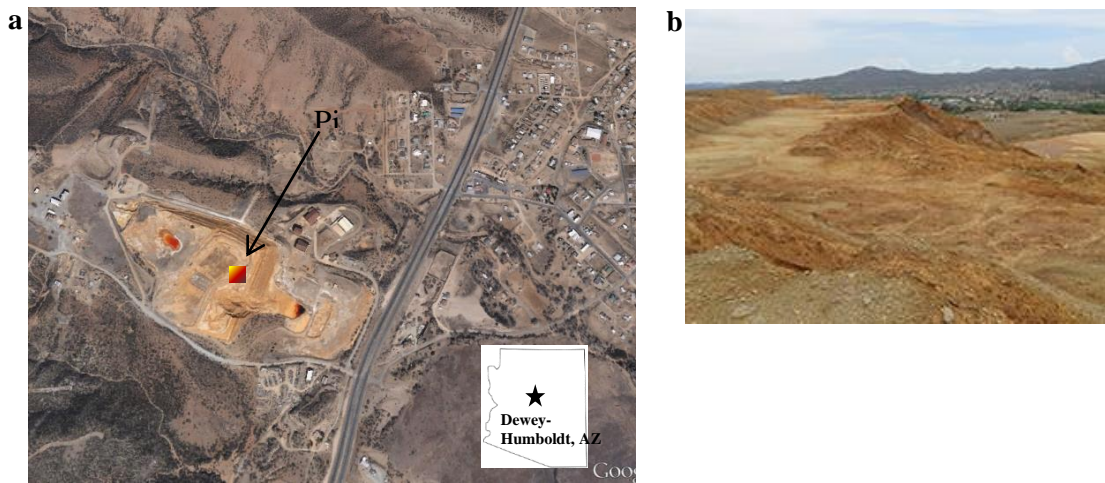


**Fig. 2** View of IKMHSS tailings pile. (a) Aerial view of tailings site and surrounding area (from Google Earth™), (b) view of tailings surface (from Arizona Department of Environmental Quality).

Since tailings application ended in 1969, the tailings surface has been subjected to over a half-century of oxidative weathering of the original gangue material, which was initially composed primarily of sulfide minerals such as pyrite ( $\text{FeS}_2$ ), arsenopyrite ( $\text{FeAsS}$ ), sphalerite ( $\text{ZnS}$ ), and galena ( $\text{PbS}$ ). Metal (loid) contaminants such as As, Pb and Zn that were already present at concentrations above remediation limits, were released from larger particulate sulfide forms during this oxidative weathering process and incorporated into colloidal precipitates that today pose a significant risk to the nearby community due to the potential for wind erosion and the spread of contaminated dust into populated areas (Csavina et al., 2012).

The tailings profile is subjected to periodic water erosion events that remove the oxidized surficial tailings and reveal the deeper zone of sulfidic particulates to potential wind and water erosion. Hence, particulate matter across the full extent of the weathering gradient is potentially susceptible to airborne transport off site. For this reason, bioaccessibility studies were conducted on the full profile of tailings material following isolation of fine particulate matter, as discussed in detail below. In addition, the results of this study may be used to predict the bioaccessibility of toxic metal (loid)s at other sites based on the extent of oxidative weathering at the surface.

## *2.2 Sample Collection and Preservation*

To examine the bioaccessibility of metal(oids) in the fine particulate matter from the IKHMSS, a tailings profile was collected by excavating a pit to a depth of approximately one meter, exposing the redox gradient from surface oxidized tailings to the reduced sulfide stable regions at depth (Figure 1). Samples were designated A-G from the surface to 1 m below the surface. Boundaries of the desired layers were determined based on color, texture, and the presence of absence of other morphological features such as concretions and cementation and approximately 20 kg of material were removed from each depth increment, homogenized and sieved to 2 mm at the site and then stored at -40°C. Samples were air-dried, with C-G depths being dried under anoxic conditions in a glove box to avoid oxidation ( $H_2:N_2 = 2:98$ , Coy, MI) prior to separation of the  $PM_{10}$  dust fraction.

## *2.3 Separation of $PM_{10}$ Fraction*

The respirable fraction of each dried sample was isolated using a laboratory dust fractionator (Figure 3), composed of a dust generation chamber, a Teflon® coated fractionation module (Cyclone PM<sub>10</sub> Model URG-2000-30EA, URG Corp., NC,), and a collection chamber (Gonzales et al., 2014). The dust generation chamber is a rotating 208 L steel drum with steel baffles bolted perpendicular to its interior surface, which facilitate mixing and resuspension of the added material. Air flowing through the center of the dust generation chamber entrained suspended particles and carried them to the cyclone fractionation module. This device separated the transported dust into two size fractions; a coarse fraction (diameter > 10 µm) and a fine fraction (diameter < 10 µm, i.e., PM<sub>10</sub>).



Fig. 3 Dust fractionator used to isolate the PM<sub>10</sub> fraction.

#### 2.4 *In vitro* Biofluids

To investigate the *in vitro* bioaccessibility of fine particulate matter (PM<sub>10</sub>) tailings, two synthetic biofluids - designed to mimic aqueous geochemical conditions in the human gastrointestinal and respiratory systems - were used. The synthetic gastric fluid (SGF) was composed of a 0.4 M glycine solution with the pH adjusted to 1.80 using reagent-grade concentrated HCl, adapted from a standard operating procedure developed by the Solubility/Bioavailability Research Consortium (SBRC, 2001). Lung fluid simulant (Takaya et al., 2006) was synthesized using a mixture of glycine and inorganic

and organic salts, with the pH adjusted to 7.4 using 1M HCl (supplementary information). Synthetic biofluids were stored at 4°C until use.

#### *2.4.1 Gastric In vitro Bioaccessibility Assays (IVBAs)*

To mimic the physiological conditions of the stomach, all gastric IVBAs were performed at 37°C maintained by a shaker incubator (Bioexpress Genemate Mini Incubator Shaker, UT) and under anoxic conditions within an anoxic chamber (Coy, MI). An aliquot of 10 mg PM<sub>10</sub> tailings from each layer was added to 1.8 mL polypropylene microcentrifuge tubes and treated with 1 mL of synthetic gastric fluid. The reaction vessels were then covered with aluminum foil to avoid chemical changes due to photocatalysis (Cornell and Schwertmann, 2003) and agitated in an end-over-end rotator within the anoxic chamber for periods between 10 s and 4 h (each time step was run in triplicate). The reactions were then terminated and solids separated by centrifugation at 5,000 g (Flexifuge, Argos) for 1 min and 0.5 mL of supernatant was aspirated and diluted in ~4.5 mL reagent-grade 0.01 M HCl (pH 2.0, same as synthetic gastric fluid). This 5 mL sample was then filtered immediately using an acid-washed Pall Acrodisk 0.2 µm syringe filter and diluted in 2% w/w HNO<sub>3</sub> for acid preservation prior to elemental analysis by inductively coupled plasma- mass spectrometry (ICP-MS, Agilent 7700, Santa Clara, CA) and  $SO_4^{2-}$  by ion chromatography (IC, Dionex, LC20 Chromatograph with ED40 Electrochemical Detector). The remaining supernatant was then aspirated and discarded and the pellet was washed in Milli-Q water, recentrifuged for one minute at 5,000 g, supernatant wash aspirated and discarded, and solid samples frozen and stored at -125°C until characterized.

### *2.4.2 Lung IVBAs*

The procedure for the lung IVBAs was similar to the gastric IVBAs, except that reactions took place under oxic conditions. After the batch reactions were terminated, the supernatant was diluted in Milli-Q water without acidification and filtered. Further dilutions were acid-preserved with 2 w/w% HNO<sub>3</sub> prior to elemental analysis using ICP-MS and IC.

## *2.5 Tailings PM<sub>10</sub> fraction characterization*

### *2.5.1 Chemical composition of PM<sub>10</sub>*

Concentrations of Fe, As, Pb and Zn in the PM<sub>10</sub> solids were determined using EPA Method 3050B for pseudo-total elemental concentrations. An aliquot of 10 mg of PM<sub>10</sub> tailings was added to a 150 mL beaker, 10 mL of 35w/w% HNO<sub>3</sub> was added. The beaker was covered with a ribbed watch glass and heated on a hot plate to ~90°C and refluxed for 15 min. After cooling, 5 mL aliquots of room-temperature concentrated (70 w/w%) HNO<sub>3</sub> were added repeatedly until fuming of NO<sub>x</sub> ceased.

The samples were cooled again and 2 mL H<sub>2</sub>O and 3 mL 30% H<sub>2</sub>O<sub>2</sub> were added to dissolve sulfides. Samples were refluxed again at ~90° C. Additions of 1 mL 30% H<sub>2</sub>O<sub>2</sub> were added until effervescence stopped. The acid-peroxide digestate was then heated until the volume of liquid had been reduced to less than 5 mL (but not allowed to dry) and cooled to room temperature. Samples were quantitatively transferred from the beakers and diluted to 100 mL with Milli-Q water particles in suspension settled and the digestate was filtered and diluted using 2% w/w HNO<sub>3</sub> for ICP-MS analysis.

### 2.5.2 Mineralogy of $PM_{10}$

X-ray diffraction data were collected on beam line 11-3 at the Stanford Synchrotron Radiation Lightsource (SSRL) operating at  $\sim 12735$  eV ( $\lambda=0.976$  Å). The instrument was operated in transmission mode with a focused spot size of  $150$   $\mu\text{m}$ , and the scans were collected using a MARCCD detector calibrated to a  $\text{LaB}_6$  standard. Prior to diffractogram collection,  $\sim 0.01$  g of unreacted and reacted  $PM_{10}$  samples were packed between two layers of clear tape (Scotch Tape<sup>TM</sup>). The samples were rastered by  $1$  mm in x and y during six 15 second exposures. Laue patterns were averaged and integrated to 2D diffractograms using the Python coded beamline software Wxdiff ([openhub.net/p/wxdiff](https://openhub.net/p/wxdiff)). The background of each scan was then manually subtracted using the xrdbs application to include contributions from X-ray amorphous phases. The patterns were converted from  $0.976$  Å to the conventional  $\text{Cu K}\alpha$   $1.54$  Å for pattern identification using the X-Pert HighScore Plus software (PANalytical).

### 2.5.3 Speciation of $PM_{10}$

#### *X-ray spectroscopic analysis*

Speciation of As, S and Fe in reacted and unreacted  $PM_{10}$  samples was analyzed with synchrotron X-ray absorption spectroscopy (XAS) on beam lines 4-3 (Fe, S) and 11-2 (As) at SSRL. A double-crystal monochromator (Si [220] crystal for As; Si [111] for Fe, S) detuned 40% to suppress higher-order harmonics was used with either a 100-element Ge detector (BL 11-2 for As) or a passivated implanted planar silicon (PIPS) detector (BL 4-3 for Fe and S) were used. Vertical slits of  $2$  mm and horizontal slits adjusted to between  $2$  and  $10$  mm were used to maximize the fluorescence signal without

saturating the detector. Energy calibration was achieved for S by designating the first peak of  $\text{Na}_2\text{S}_2\text{O}_3$  as 2472.04 eV and for Fe and As by designating the maximum of the first derivative of a Fe foil as 7112 eV and an As foil as 11,867 eV. Both Fe and As measurements were collected at  $< 77$  K using a liquid  $\text{N}_2$  cryostat used to keep the operating temperature well below the Debye temperatures for Fe (470 K) and As (282 K) (Kittel, 2005). At this temperature, spectral contributions from lattice vibrations and beam-induced chemical changes to the sample are minimized. At least three scans of all reacted and unreacted tailings samples were collected in fluorescence and transmission mode. Collection of As and Fe data was achieved with Z-1 filters with Soller slits used to minimize the contributions of elastic and Compton scattering.

Spectra data quality assessment and averaging was performed using SIXPack (v1.2; Webb, 2006). Background subtraction and normalization to the post-edge oscillations of averaged spectra was done by fitting a polynomial spline function to the linear pre-edge parameters (Fe, As: -150 eV to -30 eV) and a post-edge quadratic function extending to the end of the scanned region using the Athena program (0.9.24, Ravel and Newville, 2005).

#### *XAS Linear Combination Fits*

Linear combination fitting (LCF) of the Fe and As EXAFS and S XANES spectra were processed for quantitative analysis using Athena software (Ravel and Newville, 2005). Fits to the Fe EXAFS ( $k^3$ -weighted,  $k = 2\text{-}10 \text{ \AA}^{-1}$ ) were limited to four or less components and As EXAFS ( $k^3$ -weighted,  $k = 2\text{-}10 \text{ \AA}^{-1}$ ) to three or fewer components from a reference library of over 20 references unless other components were indicated by

secondary analysis such as XRD or FTIR (Hayes et al., 2014; Root et al., 2015). The reference spectra used were obtained from SSRL beamlines 4-3 and 11-2 under similar conditions. All LCF components were constrained to be non-negative and the sums of the components were not forced to unity. The LCF software returns a linear combination of reference standards as well as fit statistics comparing the linear combination to the actual input spectrum, and the best fits are determined by comparing the R- and  $\chi^2$ -values of each linear combination as well as the feasibility of the existence of the mineral phases in each sample.

## *2.6 Geochemical Modelling*

Aqueous data including known background electrolyte concentrations, measured total elemental concentrations, pH and  $\text{SO}_4^{2-}$  were used to calculate saturation indices of selected minerals at each measured time-point in the reaction using the SpecE8 program in Geochemist's Workbench V10.0 (Bethke, 2008). Thermodynamic data were obtained from a built-in database (thermo.dat.v8.R7) amended to include internally consistent thermodynamic constants for schwertmannite (Bigham et al., 1996) and a theoretical plumbojarosite endmember (Forray et al., 2010). Besides  $\text{SO}_4^{2-}$ , the concentrations of solution background species were not measured and were assumed to remain constant over the course of the reaction. Due to the very low solubility of Fe(III) oxide precipitates at circumneutral pH, all aqueous Fe in lung fluid was assumed to be  $\text{Fe}^{2+}_{(\text{aq})}$ . 100% of the Fe released from samples A-C, 80% released from samples D and E, and 50% released from samples F and G was designated as  $\text{Fe}^{3+}_{(\text{aq})}$  based on speciation measurements taken after two hours reaction time. All thermodynamic data used for geochemical modelling is listed in Table 1.

Mineral Name	Dissolution Reaction	25°C	40°C
Ferrihydrite	$Fe(OH)_3 + 3H^+ \leftrightarrow Fe^{3+} + 3H_2O$	3.2	2.36
Schwertmannite	$Fe_8O_8(OH)_{4.8}(SO_4)_{1.6} + 20.8H^+ \leftrightarrow 8Fe^{3+} + 1.6SO_4^{2-} + 12.8H_2O$	18	18
H-Jarosite	$(H_3O^+)Fe_3(SO_4)_2(OH)_6 + 5H^+ \leftrightarrow 3Fe^{3+} + 7H_2O + 2SO_4^{2-}$	-5.39	-7.26
Na-Jarosite	$NaFe_3(SO_4)_2(OH)_6 + 6H^+ \leftrightarrow Na^+ + 3Fe^{3+} + 7H_2O + 2SO_4^{2-}$	-5.32	-6.46
Pb-Jarosite	$Pb_{0.5}Fe_3(SO_4)_2(OH)_6 + 6H^+ \leftrightarrow 0.5Pb^{2+} + 3Fe^{3+} + 7H_2O + 2SO_4^{2-}$	-25.5	-26.1
Goethite	$FeOOH + 3H^+ \leftrightarrow Fe^{3+} + 2H_2O$	0.49	-0.02
Hematite	$Fe_2O_3 + 6H^+ \leftrightarrow 2Fe^{3+} + 3H_2O$	-1.42	-2.5
Cerussite	$PbCO_3 \leftrightarrow Pb^{2+} + CO_3^{2-}$	-13.2	-12.99
Fe (OH) <sub>2</sub> (am)	$Fe(OH)_{2(am)} + 2H^+ \leftrightarrow Fe^{2+} + 2H_2O$	13.49	12.72
Fe (OH) <sub>2</sub> (c)	$Fe(OH)_{2(c)} + 2H^+ \leftrightarrow Fe^{2+} + 2H_2O$	12.89	12.89
Siderite	$FeCO_3 \leftrightarrow Pb^{2+} + CO_3^{2-}$	-10.59	-10.65
Smithsonite	$ZnCO_3 \leftrightarrow Pb^{2+} + CO_3^{2-}$	-10.9	-10.93

**Table 1** Mineral species used for geochemical modelling and associated thermodynamic parameters.

### 3. RESULTS

#### 3.1 Characterization of Unreacted PM<sub>10</sub> Material

Sample <sup>a</sup>	Depth <sup>b</sup> (cm)	pH <sup>c</sup>	Fe <sup>d</sup> (wt%)	As <sup>d</sup> (mg kg <sup>-1</sup> )	Pb <sup>d</sup> (mg kg <sup>-1</sup> )	Zn <sup>d</sup> (mg kg <sup>-1</sup> )	Major <sup>e</sup> Components	Minor <sup>f</sup> Components
A	0-5	2.27	18.77	3030	6033	2032	qtz, jar, fh	gyp, chl, alb
B	5-20	2.31	26.23	2247	11275	1749	qtz, jar	gyp, chl, alb, fh
C	20-30	2.36	16.38	3870	8005	2939	qtz, gyp, jar, schw	chl, alb, fh
D	30-40	2.1	30.65	5773	5380	12019	qtz, gyp, jar, fh	chl, alb
E	40-52	2.92	15.06	8509	3498	6813	qtz, pyr, fh, gyp	chl, alb, jar
F	52-80	4.9	13.32	6402	5008	49889	qtz, pyr, chl	gyp, fh, ank, alb
G	80-110	5.84	15.54	4977	5695	37961	qtz, pyr, ank, chl	fh, alb

**Table 2** Chemical and mineralogical composition of the PM<sub>10</sub> fractions with depth.

<sup>a</sup> Samples labels, see Fig 1. <sup>b</sup> sampling interval below the surface. <sup>c</sup> pH <sup>d</sup> Elemental concentration measured in the indicated units. <sup>e</sup> Major components comprise  $\geq 10\%$  of the total PM<sub>10</sub> composition based on XRD and XAS results. <sup>f</sup> Other components identified using XRD and XAS results. qtz: quartz, jar: jarosite, fh: ferrihydrite, schw: schwertmannite, gyp: gypsum, chl: chlorite, ank: ankerite, alb: albite

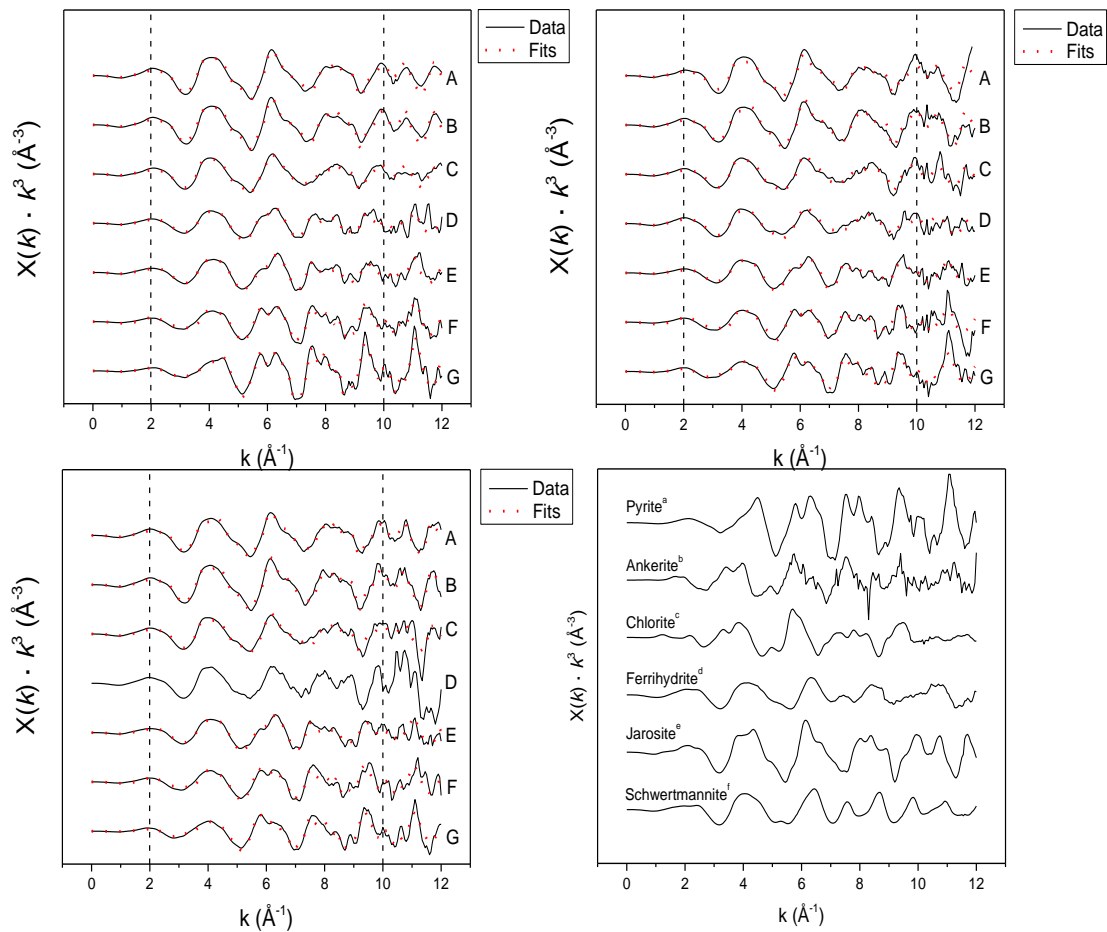


**Fig. 4** Fe K- $\alpha$   $k^3$ -weighted EXAFS sample spectra compared with linear combination fits of reference compounds. Dashed lines indicate the fit boundaries.

<sup>a</sup> Crystalline pyrite spectrum from Wards Scientific (O'Day et al., 2004b). ; <sup>b</sup> Reference ankerite from Pulaski County, AR.; <sup>c</sup> Reference chlorite (CCa-2) from Clay Mineral Society (O'Day et al., 2004b).; <sup>d</sup> Synthetic ferrihydrite prepared following Cornell & Schwertmann (2000).; <sup>e</sup> Synthetic K-Jarosite prepared following Driscoll et al. (2005) <sup>f</sup> Synthetic Schwertmannite prepared following Cornell & Schwertmann (2000).

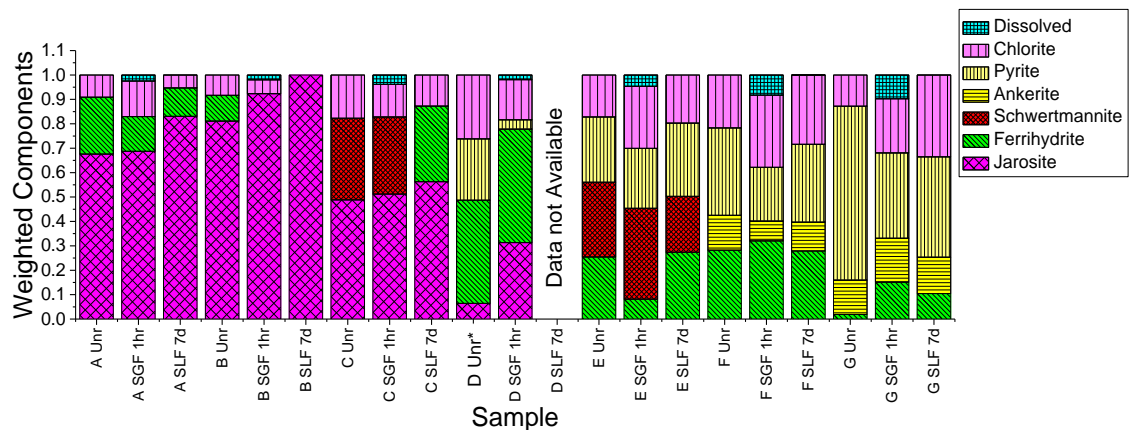


**Fig. 5**  $k^3$ -EXAFS fits showing changes in Fe speciation during lung and gastric fluid reactions.

\*This sample was slightly different from the sample of D used for the bioaccessibility assays.

**Table 3** S LCF XAS fits to S XANES spectra of unreacted and reacted samples. Fits limited to three components unless others are indicated by other methods.

<sup>a</sup> Synthetic K-Jarosite (Driscoll et al., 2005). <sup>b</sup> Standard from Wards Scientific (Alberta, Canada). <sup>c</sup> SO<sub>4</sub><sup>2-</sup> adsorbed on synthetic ferrihydrite (Cornell & Schwertmann, 2000) <sup>d</sup> Synthetic schwertmannite (Cornell & Schwertmann, 2000) <sup>e</sup> Pyrite reference from Wards Scientific (O'Day et al., 2004b).

	Jarosite <sup>a</sup>			Gypsum <sup>b</sup>			Fh-SO <sub>4</sub> <sup>c</sup>			Schwertmannite <sup>d</sup>			Pyrite <sup>e</sup>			
Sample	Weight	error	ΔE (eV)	Weight	error	ΔE (eV)	Weight	error	ΔE (eV)	Weight	error	ΔE (eV)	Weight	error	ΔE (eV)	SUM
A Unr	0.671	0.005	-	0.033	0.006	-	0.088	0.006	-	-	-	-	-	-	-	0.792
A SGF 1hr	0.745	0.003	-	-	-	-	0.072	0.002	-	-	-	-	-	-	-	0.817
A SLF 7d	0.774	0.004	-	-	-	-	0.022	0.003	-	-	-	-	-	-	-	0.796
B Unr	0.708	0.004	-	-	-	-	0.073	0.003	-	-	-	-	-	-	-	0.781
B SGF 1hr	0.702	0.003	-	-	-	-	0.079	0.002	-	-	-	-	-	-	-	0.781
B SGF 7d	0.83	0.004	-	-	-	-	0.007	0.003	-	-	-	-	-	-	-	0.837
C Unr	0.495	0.012	-	0.06	0.012	-	-	-	-	0.106	0.009	-	-	-	-	0.661
C SGF 1hr	0.675	0.01	-	-	-	-	-	-	-	0.159	0.005	-	-	-	-	0.834
C SLF 7d	0.956	0.016	0.059	-	-	-	0.034	0.012	-	-	-	-	-	-	-	0.99
D Unr	0.261	0.005	-	0.152	0.006	-	0.053	0.005	-	-	-	-	0.343	0.003	-	0.809
D SGF 1hr	0.922	0.015	-	-	-	-	0.089	0.009	-	-	-	-	0.015	0.012	-	1.026
D SLF 7d	0.974	0.016	-	-	-	-	0.097	0.009	-	-	-	-	0.015	0.013	-	1.086
E Unr	0.121	0.008	-	0.199	0.01	-	0.093	0.009	-	-	-	-	0.292	0.005	-	0.705
E SGF 1hr	0.163	0.011	-	-	-	-	0	0	-	0.173	0.006	0.114	0.623	0.005	-	0.959
E SLF 7d	0.203	0.008	-	-	-	-	0.055	0.004	-	-	-	-	0.65	0.006	-	0.908
F Unr	0.075	0.006	-	0.067	0.008	-	0.108	0.008	-	-	-	-	0.675	0.004	-	0.925
F SGF 1hr	0.048	0.004	-	-	-	-	0.036	0.003	-	-	-	-	0.866	0.004	-	0.95
F SLF 7d	0.023	0.005	-	-	-	-	0.026	0.003	-	-	-	-	0.884	0.004	-	0.933
G Unr	-	-	-	0.048	0.003	-	0.062	0.002	0.191	-	-	-	0.839	0.001	-	0.949
G SGF 1hr	-	-	-	-	-	-	0.044	0.001	0.126	-	-	-	0.887	0.005	-	0.931
G SLF 7d	-	-	-	-	-	-	0.011	0.002	-	-	-	-	0.922	0.006	-	0.933

### *3.1.1 Elemental Analysis*

The Fe, As, Pb, and Zn concentrations obtained by EPA 3050B are summarized in Table 2. The Fe concentration across the profile exhibit two maxima (B, D), corresponding to accumulations of jarosite and ferrihydrite, respectively. The As concentration reaches a maximum in the redox transition zone between 30 and 80 cm. Concentrations of Pb are at a maximum in the surface tailings (A-C), enriched to >10 g kg<sup>-1</sup> at 5-20 cm (B), and relatively depleted at 40-52 cm (E). A Zn enrichment is noted at 30-40 cm relative to shallower zones, but Zn concentrations are much higher (*ca.* 25x) in deep tailings where the pH is above 4.

### *3.1.2 Mineralogy*

The PM<sub>10</sub> particles, representing the fine fraction of the IKMHSS tailings profile, exhibited similar mineralogies to those observed in the bulk fraction (Root et al., 2015) with the PM<sub>10</sub> fractions enriched in secondary precipitates (ferrihydrite, jarosite, etc.) relative to quartz and increased concentration of associated metal(loids) (Kim et al., 2013). The compositions of the selected layers reflected a metal sulfide reaction front, with the mineralogy of the initially deposited material composed of pyrite, quartz, feldspar, chlorite and carbonates dominant in the lower layers (F, G). The layers composing the redox transition zone (D, E) exhibited compositions dominated by a mix of pyrite, quartz, ferrihydrite, carbonates, and gypsum, and the upper layers (A, B, C) were dominated by gypsum, quartz, ferrihydrite, and jarosite. Schwertmannite, a ferric hydroxysulfate, was present only at 20-30 cm. The major and minor components of layers A-G are summarized in Table 2.

### *3.1.3 Fe and As Speciation*

The Fe speciation across the tailings profile, as shown by Fe-EXAFS (Figures 4 & 5) and S-XANES (Table 3), resembled a typical pyrite weathering sequence and was consistent with the mineralogy determined by XRD (Table 2). Most of the Fe in the unweathered tailings was pyrite, with minor amounts of Fe-rich chlorite and carbonate minerals (siderite and ankerite). Shallower depths, subjected to moderate oxidative weathering show ferrihydrite as the dominant Fe phase in the transition-zone samples. In layer C, the Fe mineralogy was dominated by a mixture of jarosite and schwertmannite. At the surface, where tailings are acidic due to sulfide oxidation, the Fe phases are a mixture of jarosite and ferrihydrite.

The As in the unweathered sulfide ore tailings was arsenopyrite (FeAsS), but with increased weathering, it is oxidized and redistributed to secondary phases. In sample G (90-110 cm), very little ferrihydrite was detected. However, most of the As present at this depth in the PM<sub>10</sub> fraction was incorporated into this phase. This differs from the bulk tailings where most of the As at 1 m depth is in arsenopyrite (Root et al., 2015). Upon further oxidative weathering, revealed here as the spatial redox gradient from depth to the surface, the As was found to be incorporated into ferrihydrite and jarosite. The distribution of As solid phase speciation is shown in Figures 6 and 7.

## *3.2 Kinetic Release in Synthetic Gastric Fluid*

### *3.2.1 Arsenic*

All dissolution experiments in gastric fluid showed a similar trend of As release (Figure 8); an initial rapid release that slowly approached steady state between 15 min

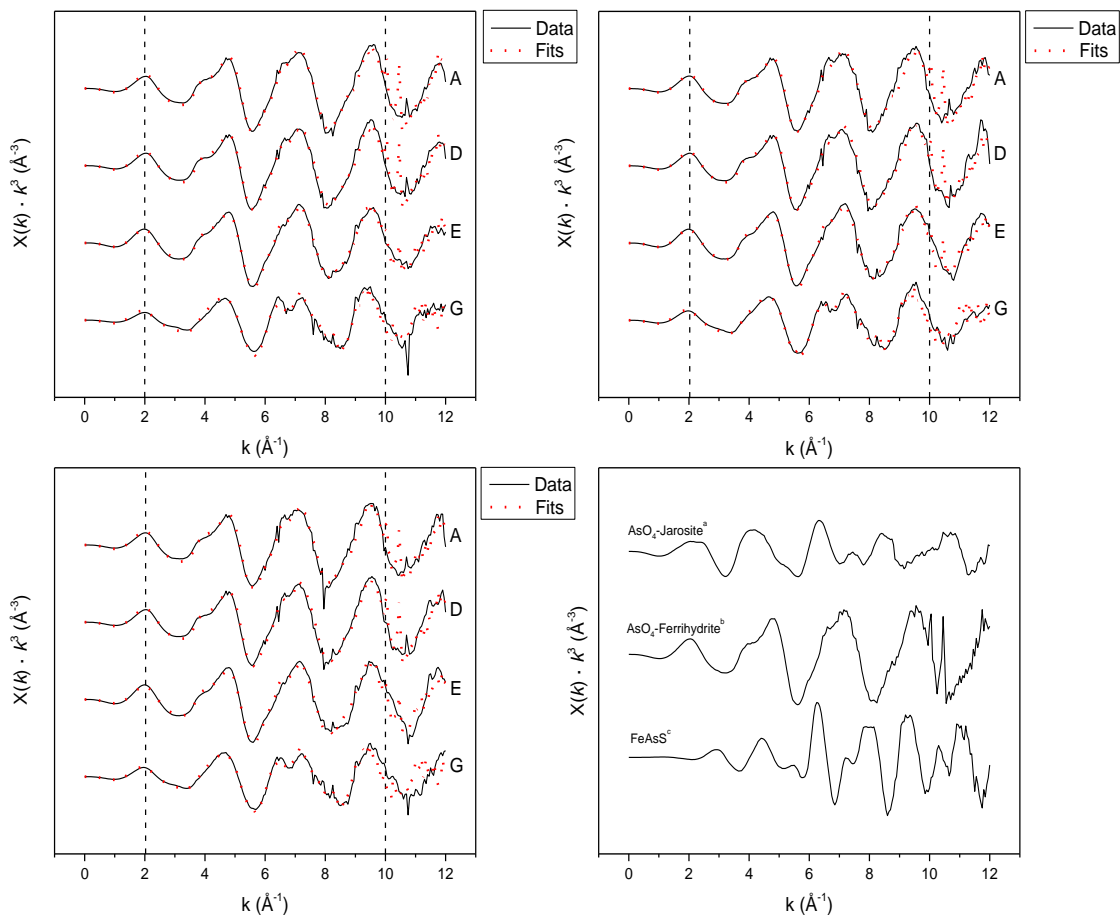


**Fig. 6** As K- $\alpha$   $k^3$ -weighted EXAFS sample spectra compared with linear combination fits of reference standards. Dashed lines indicate the fit boundaries. <sup>a</sup> Synthetic  $\text{AsO}_4^{3-}$ -bearing Jarosite synthesized following Savage et al. (2005). ; <sup>b</sup> Synthetic  $\text{AsO}_4^{3-}$ -bearing ferrihydrite synthesized following Waychunas et al. (1993). ; <sup>c</sup> Arsenopyrite reference standard from Ontario, Canada (O'Day et al., 2004a).

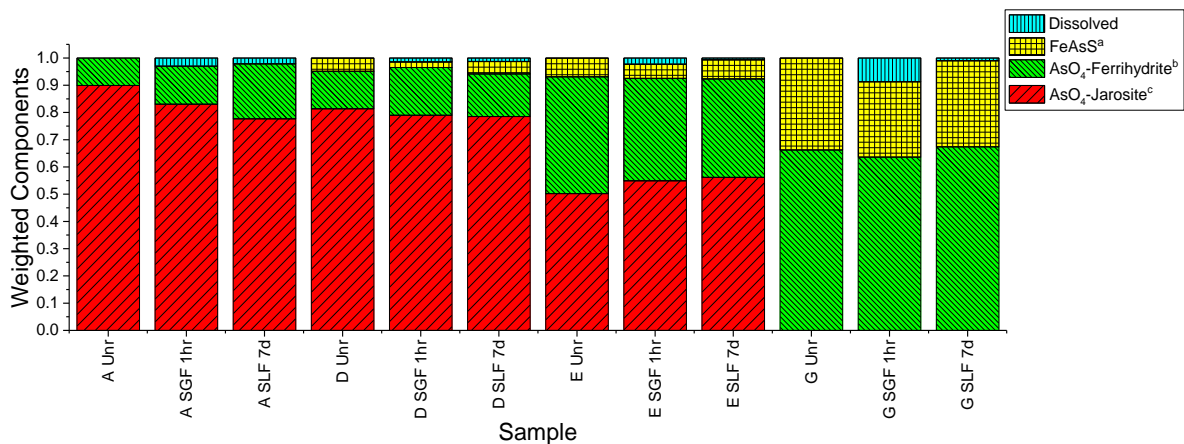


**Fig. 7**  $k^3$ -EXAFS fits showing changes in As speciation during lung and gastric fluid reactions.

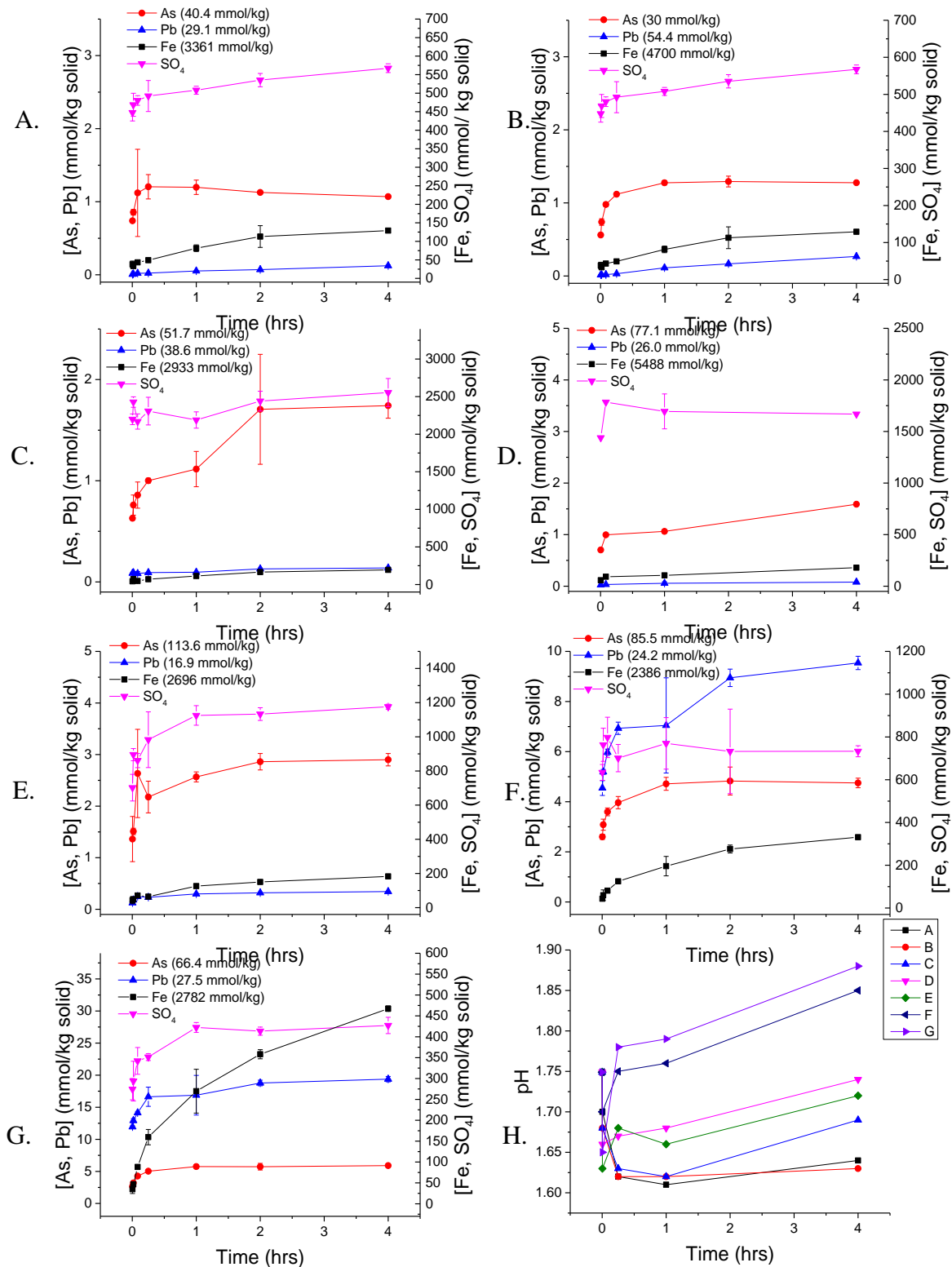


**Fig. 8** Changes in solution chemistry during SGF reactions with tailings samples A-G (charts A-G, respectively) up to four hours reaction time. All values of [As, Pb, Fe, SO<sub>4</sub>] are expressed in terms of mmol kg<sup>-1</sup> sample. Chart H shows the changes in solution pH for up to four hours reaction time.

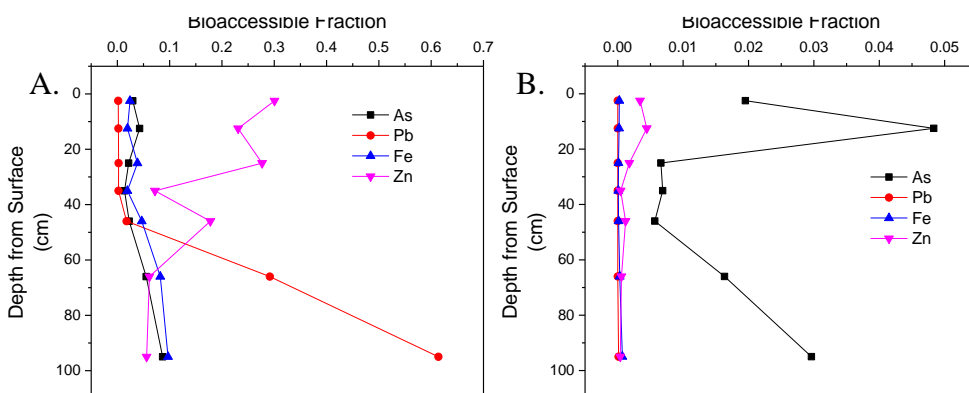


**Fig. 9** *In vitro* bioaccessibility in gastric (A) and lung (B) fluid plotted as a function of depth from the surface (cm).

Sample	Depth (cm)	Initial As Release Rate in Lung Fluid ( $\text{mmol s}^{-1} \text{kg}^{-1} \text{solid}$ )	%IVBA <sub>As</sub> in Lung Fluid	Initial Pb Release Rate in Lung Fluid ( $\text{mmol s}^{-1} \text{kg}^{-1} \text{solid}$ )	%IVBA <sub>Pb</sub> in Lung Fluid	Initial Fe Release Rate in Lung Fluid ( $\text{mmol s}^{-1} \text{kg}^{-1} \text{solid}$ )	%IVBA <sub>Fe</sub> in Lung Fluid
A	0-5	0.034	1.95%	n.d.	n.d.	0.833	0.08%
B	5-20	0.011	4.83%	n.d.	n.d.	0.183	0.16%
C	20-30	0.0093	0.66%	n.d.	n.d.	0.266	0.35%
D	30-40	0.011	0.69%	n.d.	n.d.	0.555	0.17%
E	40-52	0.015	0.57%	n.d.	n.d.	0.24	0.55%
F	52-80	0.021	1.63%	n.d.	n.d.	0.000101	0.92%
G	80-110	0.032	2.96%	n.d.	n.d.	0.000721	1.06%

**Table 4** Summary of initial elemental release rates (after 10 seconds) and percent bioaccessibilities in gastric fluid after one hour.

Sample	Depth (cm)	Initial As Release Rate in Gastric Fluid ( $\text{mmol s}^{-1} \text{kg}^{-1} \text{solid}$ )	%IVBA <sub>As</sub> in Gastric Fluid	Initial Pb Release Rate in Gastric Fluid ( $\text{mmol s}^{-1} \text{kg}^{-1} \text{solid}$ )	%IVBA <sub>Pb</sub> in Gastric Fluid	Initial Fe Release Rate in Gastric Fluid ( $\text{mmol s}^{-1} \text{kg}^{-1} \text{solid}$ )	%IVBA <sub>Fe</sub> in Gastric Fluid
A	0-5	0.074	2.96%	0.00065	0.18%	0.214	0.08%
B	5-20	0.086	4.25%	0.00145	0.21%	0.058	0.16%
C	20-30	0.112	2.16%	0.00854	0.25%	0.252	0.35%
D	30-40	0.121	1.38%	0.00244	0.22%	0.411	0.17%
E	40-52	0.12	2.26%	0.0124	1.76%	0.611	0.55%
F	52-80	0.113	5.52%	0.455	29.20%	0.616	0.92%
G	80-110	0.107	8.65%	0.458	61.40%	0.529	1.06%

**Table 5** Summary of initial elemental release rates and percent bioaccessibilities in lung fluid after seven days.

and 1 h after the beginning of the reaction. After normalizing of the kinetic data by dividing by the total initial As concentrations, the gastric bioaccessibility of As at 1 h, a time point used for comparison across SGF release, ranged from 1.4% for sample D to 8.7% for sample G. In general, the deeper sulfidic tailings layers (F, G) showed the highest gastric As bioaccessibility, followed by the surface layers (A, B), with the layers comprising the redox transition zone (C, D & E) showing the lowest values. All initial release rates (calculated from the amount of each element released in the first 10 s) and equilibrium values of gastric bioaccessibility are recorded in Table 4, while Figure 9 relates gastric bioaccessibility to depth. Although C, D and E showed the most rapid initial release rates (0.11-0.12 mmol s<sup>-1</sup> kg<sup>-1</sup> solid, slightly higher than that other samples), the equilibrium gastric bioaccessibilities of these samples were lower than all of the other tested samples.

### 3.2.2 Lead

In contrast to As release kinetics, Pb release kinetics varied dramatically from sample to sample. Pb<sup>2+</sup><sub>(aq)</sub> release from samples A through E showed a small initial release of less than 0.01 mmol s<sup>-1</sup> kg<sup>-1</sup> solid (Table 4) followed by a steady decrease in reaction rate until reaching apparent equilibrium (Figure 8). On the other hand, samples C, F and G showed a large initial release in the first 10 s of greater than 40% of the total Pb dissolved in the course of the reaction, after which the Pb<sub>(aq)</sub> concentration increased gradually before reaching equilibrium. The total gastric bioaccessibility of Pb after 1 h also varied widely between samples (Table 4, Figure 9), ranging from 0.18% for A to 61.4% for G.

### 3.2.3 Iron

Iron was released into gastric fluid at a rate considerably higher than that observed for Pb (Figure 8), an observation attributed to the very high Fe concentrations in the fine fraction across the tailings profile. After an initial release of  $\text{Fe}_{(\text{aq})}$  into solution that varied in magnitude from  $0.058 \text{ mmol s}^{-1} \text{ kg}^{-1}$  for sample B to  $0.616 \text{ mmol s}^{-1} \text{ kg}^{-1}$  for sample F (Table 4), the  $\text{Fe}_{(\text{aq})}$  concentration did not appear to reach equilibrium over the course of the gastric fluid treatment. The gastric bioaccessibility after one hour of reaction time ranged from 1.92% for sample D to 9.69% for sample G (Table 4, Figure 9).

### 3.2.4 Sulfate

Sulfate release into gastric fluid depended on the depth at which the samples were collected and was much higher from the transition zone samples than the others. All of the samples showed a large initial release of  $\text{SO}_4^{2-}$  in the first 10 s of reaction, but the magnitude of this release was highest in samples C, D and E, where x-ray diffraction indicated the largest proportion of sulfate salt, e.g. gypsum (Figure 8). Following this initial release, sulfate concentrations in the extraction fluid continued to increase for all of the samples and reached apparent equilibrium between 15 min and 2 h, depending on the sample (Figure 8). Also, the concentration of sulfate in the D gastric fluid reaction decreased by approximately 65% between 1 and 4 h after the reaction began.

### 3.2.5 pH

The dissolution/precipitation reactions occurring during reaction of tailings material with gastric fluid consume or release  $\text{H}^+$  and  $\text{OH}^-$  ions, therefore pH

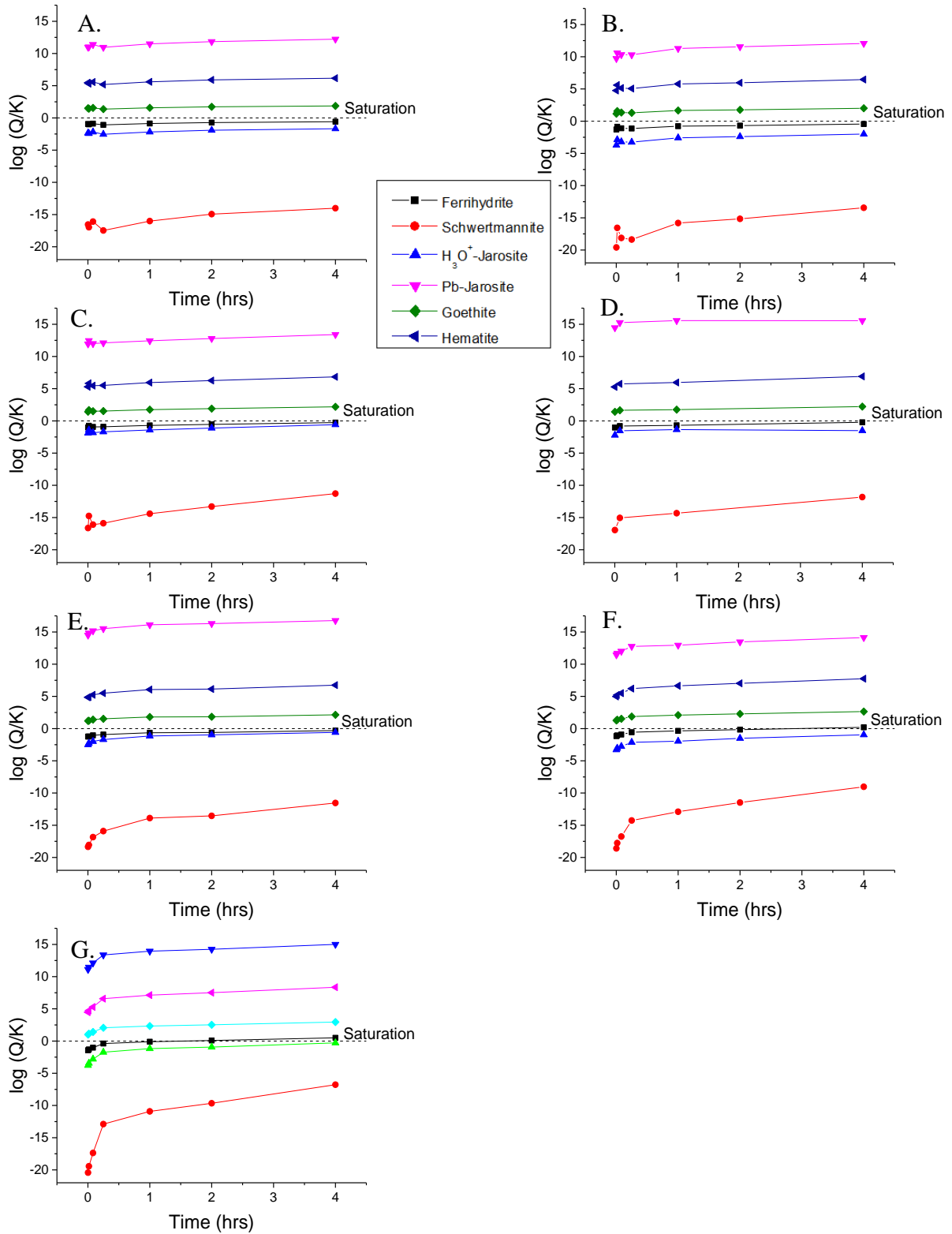


**Fig. 10** Time-dependent saturation indices (SI= $\log(Q/K)$ ) of selected mineral species in gastric fluid reacted with samples A-G (charts A-G, respectively) up to four hours reaction time.

measurements at each time point in the reaction were recorded (Figure 8). After an initial decrease in pH following tailings addition to gastric fluid, which was more pronounced in the acidic surface tailings, the pH increased progressively until the reaction was terminated after 4 h. This observed increase in pH was greater for the sulfidic tailings than those oxidized tailings found at the surface.

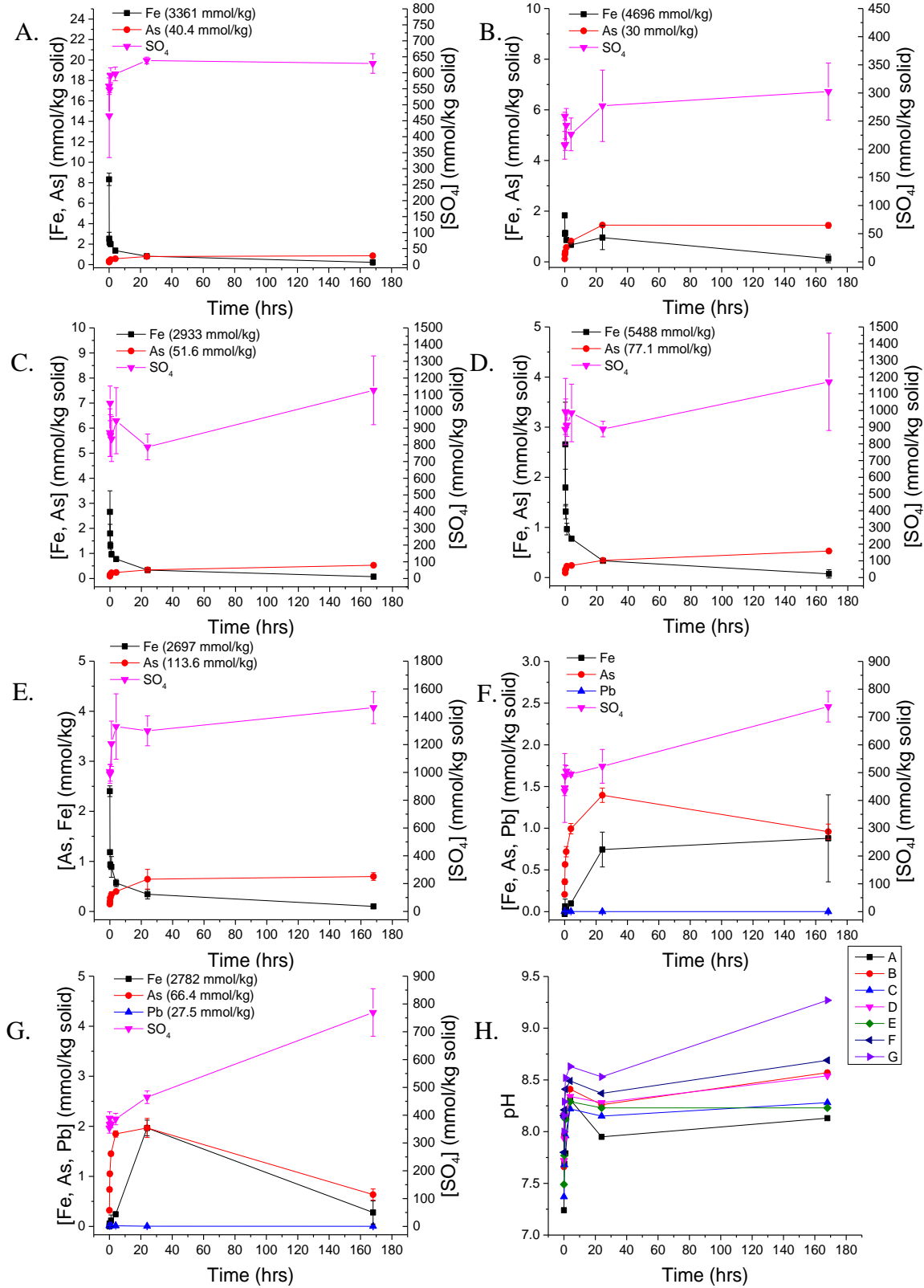
### ***3.2.6 Geochemical Modelling Results***

Figure 10 shows how the saturation indices of selected Fe(III) oxyhydroxide and oxyhydroxysulfate species in reacted gastric fluid evolve over time. As  $\text{Fe}^{3+}$  is released from all samples, ferrihydrite approaches saturation asymptotically, while no precipitation of goethite or hematite was observed even though the solutions were supersaturated relative to these minerals. The saturation indices of various jarosite endmembers were also calculated;  $\text{H}_3\text{O}$ -jarosite stayed below saturation in all samples while an insoluble theoretical plumbojarosite hypothesized by Forray et al. (2010) had a saturation index  $>10$  in all samples. Schwertmannite was undersaturated ( $S \leq -8$ ) in all samples based on a dissolution reaction hypothesized by Bigham et al. (1996); however, this is unlikely because schwertmannite is thermodynamically-favored over ferrihydrite under acidic conditions (Regenspurg et al., 2004).

## ***3.3 Reaction Kinetics in Synthetic Lung Fluid (SLF)***

### ***3.3.1 Arsenic***

After normalizing As release over the 7 d reaction to the total concentration of As in each solid, all dissolution experiments showed a similar trend in the first 24 h (Figure 11); an initial rapid release followed by a gradual increase in As concentration before As



**Fig. 11** Changes in solution chemistry during SLF reactions with samples A-G (charts A-G, respectively) up to seven days reaction time. All values of [As, Pb, Fe, SO<sub>4</sub>] are expressed in terms of mmol kg<sup>-1</sup> sample. Chart H shows the changes in solution pH for up to seven days reaction time.

concentrations reached apparent equilibrium between 4 and 24 hours. However, the aqueous concentration of As in equilibrium with samples F and G showed large decreases of 30% (F) and 70% (G) after 24 h, a feature that was not observed in the other tailings samples.

As a time point for comparison across SLF IVBA, the extracted metal (loid) at 24 h was highlighted. The lung bioaccessibility of As after 24 h ranged from 0.57% for sample E to 4.83% for sample B. In general, the oxidized surface tailings (A, B) showed the highest gastric bioaccessibility of As, followed by the reduced layers (F, G), with the layers comprising the redox transition zone (C, D & E) showing the lowest values. All initial release rates and equilibrium values of alveolar bioaccessibility are recorded in Table 5 and Figure 9.

### 3.3.2 Lead

Samples A-E showed no detectable releases of Pb into lung fluid because concentrations were below the ICP-MS detection limit (method detection limit  $\sim 10 \mu\text{g kg}^{-1}$ ). Treatment of samples F and G with lung fluid lead to an initial Pb release of up to  $0.0012 \text{ mmol s}^{-1} \text{ kg}^{-1}$  before reaching equilibrium at a very low  $\text{Pb}_{(\text{aq})}$  concentration near the limit of detection (Figure 11). Because Pb lung bioaccessibility was found to be unquantifiable for samples A-E, release and equilibrium percent bioaccessibility values are not reported for Pb in lung fluid.

### 3.3.3 Iron

The Fe release from samples A-E into lung fluid displayed similar kinetic behavior to  $\text{Pb}_{(\text{aq})}$ , with an initial release of 0.183 (B) to 0.833 (A)  $\text{mmol kg}^{-1} \text{ s}^{-1}$  followed

by a decrease to equilibrium concentrations after approximately 4-24 h (Figure 11).

Samples F and G released Fe to lung fluid at a low initial rate, but the  $\text{Fe}_{(\text{aq})}$  concentration eventually reached apparent equilibrium at a slightly higher level than Fe released from the other solids. Solution phase Fe concentrations for sample G then decreased by about 85% between 24 h and 7 d after the reaction began. Initial release rates and equilibrium percent bioaccessibilities of Fe in lung fluid are recorded in Table 5 and Figure 9.

### *3.3.5 Sulfate*

Sulfate is a constituent in the synthetic alveolar fluid used at concentration of approximately 560  $\mu\text{M}$ . Sulfate released from all samples into lung fluid showed a large initial release of over 80% of all sulfate dissolved over the course of the reaction (Figure 11). Afterwards, sulfate release from samples A, B and D reached apparent equilibrium after about 24 h, while release from samples C, E and F continued to increase until the end of the reaction.

### *3.3.6 pH*

The pH at each time point after addition of the tailings samples to synthetic lung fluid was also measured (Figure 11). All reactions showed an initial decrease in pH immediately after the samples were added, followed by a steady increase in pH as the reaction progressed before termination after 7 d. This increase in pH was highest for the deeper sulfidic tailings samples F and G, resulting in highly alkaline aqueous phases, with pH of each reaction increasing to above 8.7 at the end of these experiments. This increase in pH occurred as Fe and As solution concentrations decreased simultaneously.

### *3.3.7 Geochemical Modelling Results*

After designating all of the  $\text{Fe}_{(\text{aq})}$  detected in the reacted lung fluid as  $\text{Fe}^{3+}_{(\text{aq})}$ , the calculated saturation indices of ferrihydrite, goethite, hematite and K-Jarosite were all supersaturated at the beginning of the reaction, with the saturation index decreasing as  $\text{Fe}_{(\text{aq})}$  precipitated out of solution (Figure 12). The saturation index of ferrihydrite remained above 5 in all reactions. When all of the measured  $\text{Fe}_{(\text{aq})}$  was designated as  $\text{Fe}^{2+}_{(\text{aq})}$ , the saturation indices of minerals such as metal carbonates (cerussite, smithsonite and siderite) and amorphous and crystalline Fe (II) hydrolysis products were calculated. Supersaturation of the metal carbonate minerals was observed in all reactions, especially within the first hour of reaction time, and supersaturation of the Fe (II) hydrolysis products was observed after treatment of sample G with lung fluid (Figure 13).

### *3.4 Changes in IVBA Reacted Solid $\text{PM}_{10}$ Samples*

#### *3.4.1 Near Surface $\text{PM}_{10}$ in Gastric Fluid*

The mineralogical composition of the surface samples (Figure 14A) included quartz, jarosite, gypsum, ferrihydrite and chlorite prior to introduction into gastric fluid. The gypsum, and presumably other efflorescent sulfate salts dissolved upon introduction into gastric fluid. The diffraction peaks assigned to jarosite in samples A and C also decreased at the first 10 s time step, followed by alternating periods of jarosite dissolution and precipitation until the reaction was terminated after 4 h (see supplementary data). Fe XAS, however, showed an increase in jarosite following reaction with gastric fluid and a simultaneous decrease in ferrihydrite and/or schwertmannite (Figures 4 & 5). The most dramatic change was observed in sample B, where no ferrihydrite was detected with Fe

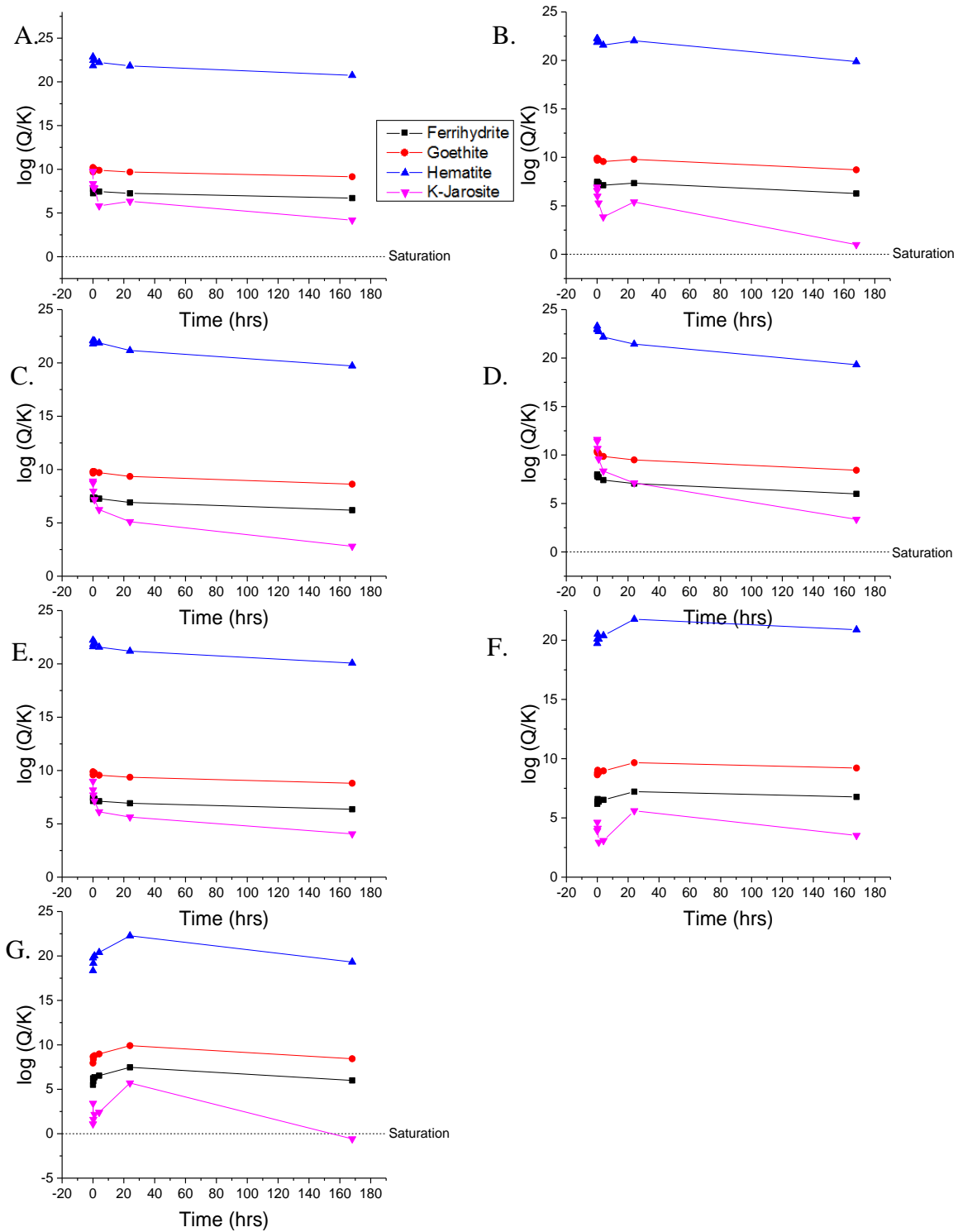


**Fig. 12** Time-dependent saturation indices (SI= $\log(Q/K)$ ) of selected mineral species in lung fluid reacted with sample A-G (charts A-G, respectively) up to seven days reaction time. All  $Fe_{(aq)}$  is assumed to be  $Fe^{3+}$ .

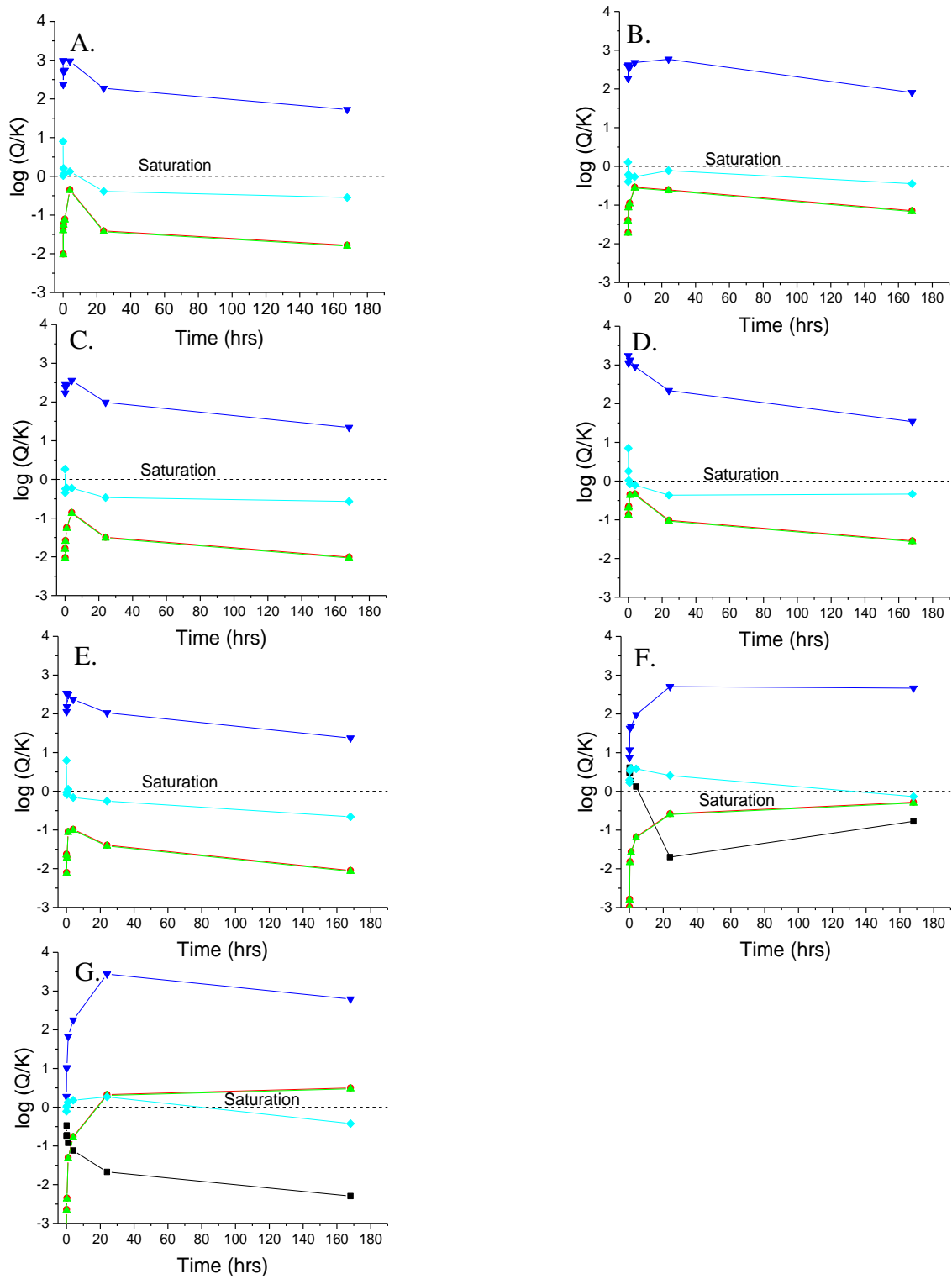


**Fig. 13** Time-dependent saturation indices ( $SI = \log(Q/K)$ ) of selected mineral species in lung fluid reacted with sample A-G (charts A-G, respectively) up to seven days reaction time. All  $Fe_{(aq)}$  is assumed to be  $Fe^{2+}$ .

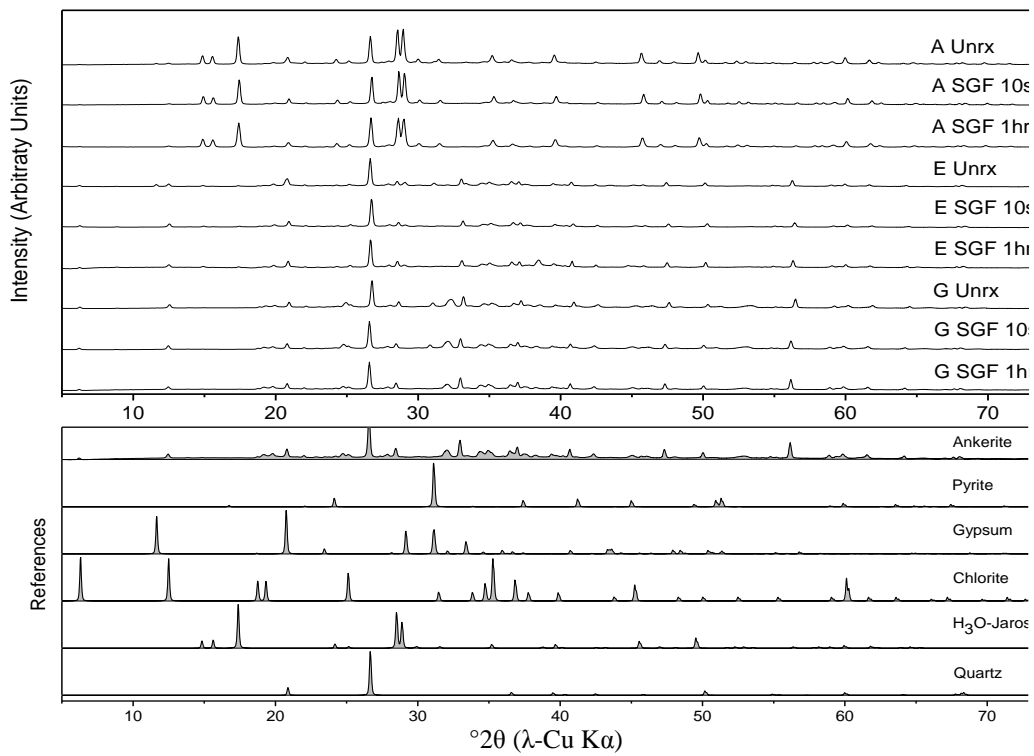


**Fig. 14** X-ray diffractograms showing mineralogical evolution of samples A, E, and G during gastric fluid reactions.

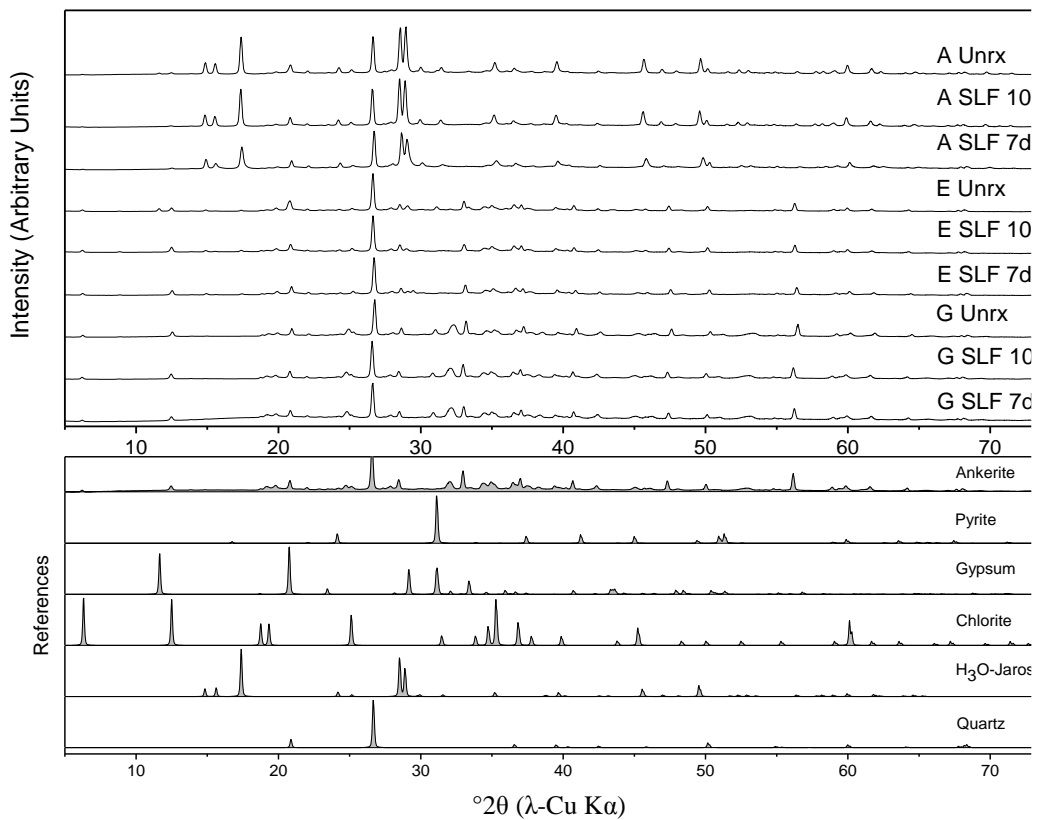


**Fig. 15** X-ray diffractograms showing mineralogical evolution of samples A, E, and G during lung fluid reactions.

XAS after one hour of reaction time. On the other hand, As XAS showed redistribution of arsenate from jarosite to ferrihydrite (Figure 6, 7). Quartz diffraction peaks showed minimal change during the gastric fluid assay, but the chlorite peaks decreased in sample B.

#### **3.4.2 Redox Transition-zone $PM_{10}$ in Gastric Fluid**

Prior to treatment with synthetic gastric fluid, the sub-oxic transition-zone samples (Figure 14E) were composed of a mix of pyrite, ferrihydrite, quartz, gypsum, and a minor amount of jarosite. The sulfate salt fraction of these samples dissolved immediately after the addition of gastric fluid. XRD results for sample E showed a loss of jarosite from the sample (Figures 5, 14), and no jarosite was detected in E after the gastric fluid assay. On the other hand, jarosite precipitation was observed after sample D was reacted with gastric fluid, and schwertmannite precipitation in sample E was indicated by Fe EXAFS and S XANES (Figure 5, Table 3). In sample E, both ferrihydrite and schwertmannite were included as components. The behavior of As in the transition zone samples varied by sample; D showed redistribution of As from jarosite to ferrihydrite in gastric fluid, while E showed As redistribution into jarosite (Figures 6, 7).

#### **3.4.3 Deep Unweathered $PM_{10}$ in Gastric Fluid**

The unweathered samples F and G were composed primarily of pyrite, quartz, carbonates, chlorite and small amounts of ferrihydrite and gypsum (Table 2). As observed when the other samples were reacted with gastric fluid, the sulfate salts in these samples dissolved immediately, followed by further dissolution of the carbonates, pyrite and ferrihydrite present in both samples (Figure 14G). Carbonate dissolution occurred at a

slower rate than dissolution of ferrihydrite and pyrite and Fe EXAFS showed a relative increase in ankerite after 1 h, although this increase was within the 0.05 standard error of an EXAFS LCF fit (Figure 5). The ankerite XRD peaks also persisted until this time point but had lower amplitudes. Jarosite and schwertmannite precipitation were not observed during either reaction. Following treatment of these samples with gastric fluid, As redistribution from arsenopyrite to ferrihydrite was observed with XAS (Figure 7).

#### *3.4.4 Surface PM<sub>10</sub> in Lung Fluid*

The effluorescent sulfate salts in the surface samples dissolved immediately upon introduction into synthetic lung fluid. Iron EXAFS showed that the poorly-crystalline Fe component decreased and the jarosite component increased in all surface samples over the course of the lung fluid assay (Figure 5). Because S XANES showed that the schwertmannite component was removed over the course of the lung fluid reaction (Table 3), the entire poorly-crystalline Fe component in the Fe XAS fits was assigned to ferrihydrite. As speciation with XAS showed As redistribution from jarosite to ferrihydrite in sample A, the magnitude of which was greater than observed in gastric fluid (Figure 7).

#### *3.4.5 Redox Transition-zone PM<sub>10</sub> in Lung Fluid*

Sulfur XANES of sample D and E indicated that the dominant change in mineralogy after exposure to lung fluid was the dissolution of sulfate salts. These samples also showed a decrease in the pyrite and ferrihydrite components and an increase in the jarosite component of the Fe XAS fit (Table 3, Figure 5). Fe EXAFS results for sample D reacted in lung fluid are unavailable, but no statistically significant changes in Fe

speciation were observed in sample E (Figure 5). No statistically significant changes in As speciation were observed in sample D, but As XAS spectra of sample E showed redistribution of  $\text{AsO}_4^{3-}$  from ferrihydrite to jarosite (Figure 7).

#### ***3.4.6 Deep Unweathered $\text{PM}_{10}$ in Lung Fluid***

Prior to treatment with synthetic lung fluid, samples F and G were dominated by pyrite, quartz, ankerite and chlorite, with some ferrihydrite observed in sample F. The quartz, chlorite and ankerite XRD peaks did not decrease in size over the course of the reaction, but a decrease in pyrite was observed with both XRD and XAS, which showed a decrease in the pyrite component and an increase in the ferrihydrite component (Figure 5, Figure 15G). No jarosite phases were detected using XRD or Fe XAS (Figure 5), and no statistically significant changes in As speciation were observed with As XAS (Figure 7).

## **4. Discussion**

### ***4.1 Mineralogical and Morphological Characterization of the Tailings Fine Fraction***

#### ***4.1.1 Unweathered Tailings***

The mineralogical, chemical and morphological characteristics of the fine fraction of each sample were determined. This characterization showed that the composition of the fine particle fraction in each layer was a result of 1) the proportion of fine particles in the unweathered parent material, 2) secondary precipitates in the fine fraction that form as a result of oxidative weathering, and 3) illuviation and immobilization of particles and solutes from upper layers of the tailings profile.

In the absence of oxidative weathering, the PM<sub>10</sub> fraction of the tailings is dominated by pyrite, quartz, chlorite and carbonate fragments generated by anthropogenically enhanced physical weathering (Table 2). Although Fe in these samples are concentrated primarily in sulfide, carbonate and chlorite phases (Figure 5), small amounts of secondary precipitates present in the samples suggest that incipient weathering processes have contributed secondary precipitates such as As-bearing Fe(III) oxyhydroxides and oxyhydroxysulfate salts in the fine fractions that are not observed in the bulk tailings (Hayes et al., 2014).

#### *4.1.2 Partially-Oxidized Tailings*

The partially-oxidized tailings samples (D and E) were composed of a mixture of primary minerals and secondary mineral products, with secondary precipitates becoming increasingly dominant as oxidative weathering processes continue. Pyrite, ankerite, and chlorite are depleted relative to the unweathered tailings samples, and ferrihydrite, the initial secondary phase produced by pyrite oxidation, is the dominant phase in samples D and E. The cementation that was observed in the partially-oxidized layers *in situ* is most likely a result of precipitation of ferrihydrite in this region.

Total elemental concentrations in the partially-oxidized samples (Table 2) show enrichment of Fe and As in the fine fraction compared to the surface and unweathered tailings samples. Iron enrichment reaches 30.6% in sample D (compared to 16.4% in the layer above, indicating either concentration of Fe(III) secondary precipitates in the fine fraction or precipitation of leached Fe(III) from the surface. Hayes et al. (2014) observed Fe enrichment in the bulk fraction of partially-oxidized layers from a similar pit at the

IKMHSS tailinngs site, suggesting that Fe(III) leaching is the primary process contributing to Fe enrichment in these samples. Arsenic enrichment is particularly pronounced in sample E, most likely due to the dominance of this layer by ferrihydrite . Arsenic is known to be associated with ferrihydrite (Waychunas, et al.), and ferrihydrite partitioning into the PM<sub>10</sub> fraction is probably a major factor contributing to As enrichment in the partially-oxidized PM<sub>10</sub> samples. This may have an effect on the IVBA of As in this layer, as As-loaded ferrihydrite is known to dissolve slowly in HCl (Paige et al., 1997).

#### *4.1.3 Surface Tailings*

Oxidative weathering of sulfides in the fine fractions of samples A, B and C is complete, with no remaining sulfides detected. As a result, this portion of the tailings profile is highly acidic, leading to the transformation of ferrihydrite into Fe(III) oxyhydroxysulfate phases. Hydroniumjarosite [(H<sub>3</sub>O<sup>+</sup>) Fe<sub>3</sub>(OH)<sub>6</sub>(SO<sub>4</sub>)<sub>2</sub>] and schwertmannite [Fe<sub>8</sub>O<sub>8</sub>(OH)<sub>6</sub>(SO<sub>4</sub>)·nH<sub>2</sub>O] are the most common minerals observed in these samples, and they are more thermodynamically stable under the high acidity, high-sulfate conditions found at the tailings surface. However, ferrihydrite was found to persist in these samples, most likely due to the semi-arid conditions at the site (Hayes et al., 2014). Low water content at the tailings surface leads to hypersaline conditions in the pore water, preventing solvation of ferrihydrite and allowing the persistence of efflorescent salts such as gypsum, which was also observed in the surface samples. Gypsum was especially common in sample C, most likely as a result of sulfate leaching from the upper layers and incomplete transformation to jarosite and schwertmannite.

Interestingly, the surface tailings sample A showed a persistence of ferrihydrite even though this layer has been exposed to oxidative weathering for decades. The fine fraction in A consists of a higher proportion of ferrihydrite than samples B or C, a feature that was not observed in studies of bulk tailings samples at Iron King (Hayes et al., 2014). It is possible that this difference is caused by concentration of ferrihydrite in the fine fraction in sample A, as ferrihydrite aggregation is limited under acidic conditions (Cismasu et al., 2011), especially when the activity of counter-ions such as sulfate has been reduced by gypsum and jarosite precipitation. However, it is also plausible that it formed due to runoff from precipitation events. Dissolved ferrous iron in the acid runoff may have been transported to the sampling site and precipitated due to changes in pH or alternating wet-dry cycles.

#### *4.4 Factors Controlling Gastric Bioaccessibility*

This experiment showed that gastric bioaccessibility of trace elements in PM<sub>10</sub> fine fraction is determined by the chemical and mineralogical compositions of the solid and aqueous phases. Specifically, trace elements are released into solution by dissolution and desorption processes taking place at solid-solution interfaces and removed from solution by coprecipitation and adsorption; therefore, the kinetics of contaminant release into solution are determined by mineralogical changes in the solid phase over time and supersaturation of neo-phases in the aqueous fraction as a result of reaction with biofluids. The factors found to control these mineralogical changes and, by extension, trace element concentrations in solution included oxidation state and activity of Fe and S, sulfate site activity, and the presence of nucleation sites for precipitation of new surfaces.

#### *4.4.1 Fe Oxidation State*

Fe(III) oxides and oxyhydroxysulfates, which are major byproducts of sulfide mineral oxidation, have been found to be important sinks for trace elements, especially As (Root et al., 2015; Foster et al., 1998; Sherman and Randall, 2003; Paktunc et al., 2004) and Pb (Ostergren et al., 1999; Morin et al., 1999; Hayes et al., 2009; Root et al., 2015). These phases require high  $\text{Fe}^{3+}_{(\text{aq})}$  activity and supersaturation for nucleation and crystal growth. The deep, unweathered tailings samples (F & G) have Fe mineralogies dominated by ferrous sulfides and carbonates. Secondary ferrous minerals are more soluble than ferric counterparts, and the  $\text{Fe}^{2+}$  released by acid dissolution of these minerals is unable to drive the formation of ferric As- and Pb-bearing precipitates such as ferrihydrite and jarosite. Metal carbonates are also highly soluble under acidic conditions and are able to quickly release solutes into solution, while metal sulfides were found to be surprisingly soluble under acidic, low- $f\text{O}_2$  conditions. Acid volatilization of sulfides under these conditions may have occurred, but was not confirmed by  $\text{H}_2\text{S}$  release.

#### *4.4.2 Adsorbent Surfaces*

The sub-oxic transition samples were consistently found to have the lowest As bioaccessible fraction of all samples tested in this study. This is attributed to higher levels of short range-order Fe(III) oxides and oxyhydroxysulfates, such as ferrihydrite and schwertmannite, observed in these samples. Synthetic ferrihydrite and schwertmannite have a high capacity for sorption of  $\text{H}_2\text{AsO}_4^{-}(\text{aq})$  (Raven et al., 1998; Burton et al., 2009) and a limited capacity for  $\text{Pb}^{2+}(\text{aq})$  sorption (Webster et al., 1998) under acidic conditions. The higher proportion of high-surface area amorphous metal oxide phases in the transition-zone samples means that adsorption to these surfaces may lower the

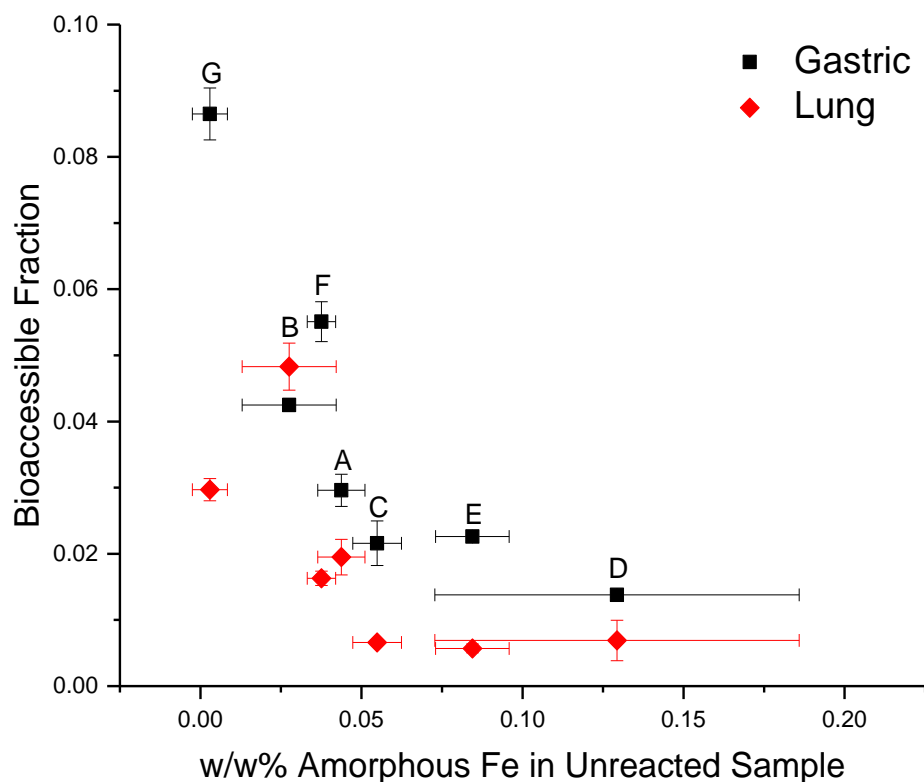


**Fig. 16** Relationship of As bioaccessible fraction in lung and gastric fluid to the w/w% of Fe in amorphous Fe(III) oxyhydroxides (w/w% amorphous Fe = w/w% Fe \* amorphous Fe EXAFS fit). Standard errors calculated from measured experimental error.

bioaccessibility of trace elements (especially As). Figure 16 relates the As bioaccessible fraction to the amount of ferrihydrite and/or schwertmannite in each sample prior to reaction with lung or gastric fluid. There is a strong negative correlation between the two factors, with the exception of a single outlier in the lung fluid (sample B, where no ferrihydrite was detected after treatment with lung and gastric fluid). In addition, prior work has shown that ferrihydrite with coprecipitated and/or adsorbed  $\text{H}_2\text{AsO}_4^-$ , as observed in samples D and E, has a slower dissolution rate in HCl than pure ferrihydrite (Paige et al., 1997). Because  $\text{H}_2\text{AsO}_4^-$  forms bidentate binuclear complexes on ferrihydrite surfaces (Waychunas et al., 1993), it links and protects Fe(III) centers and thereby diminishes the rate of proton- and ligand-promoted dissolution of ferrihydrite

(Paige et al., 1997) and potentially other Fe(III) oxides. Incorporation of arsenate and other trace element species (Regenspurg & Peiffer, 2005) has also been shown to retard the dissolution of schwertmannite.

#### *4.4.3 Sulfate Salts*

An accumulation of evaporite sulfate salts, especially gypsum ( $\text{CaSO}_4 \cdot 2\text{H}_2\text{O}$ ), was observed in the transition-zone  $\text{PM}_{10}$  samples due to sulfate and metal cation leaching from the surface horizons, or capillary wicking from deeper tailings. When these samples were introduced into gastric fluid, they dissolved immediately and released  $\text{SO}_4^{2-}$  to solution, which, along with  $\text{Fe}^{3+}_{(\text{aq})}$ , drives precipitation of jarosite and potentially other alunite minerals (such as beudantite  $[\text{PbFe}_3(\text{OH})_6\text{SO}_4\text{AsO}_4]$  and segnitite  $[\text{PbFe}_3(\text{AsO}_4)_2(\text{OH}, \text{H}_2\text{O})_6]$  (Dutrizac & Jambor, 2000)). Arsenate and lead incorporation into these newly-precipitated minerals further decreases the percent bioaccessibility in samples with high levels of sulfate salts compared to samples F and G, which have very low levels of sulfate salts because the sulfide parent material has not been oxidized. Pb bioaccessibility had a stronger dependence on jarosite precipitation than As bioaccessibility, most likely due to the insolubility of Pb-bearing jarosite (Kashkay et al., 1975; Forray et al., 2010). As release from jarosite in sample A was indicated by As EXAFS even though jarosite was precipitating, indicating that ferrihydrite may have been a more important sink for As in the surface samples. In the absence of Pb speciation data, it is unknown whether the low Pb bioaccessibility in the jarosite-dominated samples is due to the recalcitrance of existing plumbojarosite or due to the formation of secondary Pb-bearing jarosites during the reaction.

#### *4.4.4 Nucleation and Growth of Jarosite Crystals*

Although the presence of aqueous sulfate as a thermodynamic driver of jarosite precipitation was an important factor controlling trace element bioaccessibility in this study, there were kinetic limitations to jarosite precipitation that affected bioaccessibility in some of the samples. Jarosite is a long-range-ordered, crystalline mineral with a high surface energy (Morse & Casey, 1988; Yang et al., 2015), and there are therefore kinetic limitations to homogenous nucleation even under acidic, high-sulfate conditions when jarosite formation is thermodynamically favorable (Beckmann, 2013). In the absence of existing crystal template surfaces that allow heterogenous nucleation and crystal growth, amorphous precipitates such as schwertmannite with lower surface energies are instead initially favored, and then are eventually transformed to the more crystalline jarosite (Morse & Casey, 1988). In samples where jarosite is present, precipitation was observed to occur via growth of existing crystals, but in sample E, where most of the jarosite dissolves in gastric fluid, schwertmannite formation was indicated by Fe-EXAFS and S-XANES, although the solution was supersaturated relative to a Pb-bearing jarosite precipitate, and the calculations indicated that the solution was undersaturated relative to schwertmannite. Because schwertmannite is a less effective sink for As and Pb than ferrihydrite or jarosite, respectively (Carlson et al., 2002; Acero et al., 2006), this results in increased bioaccessibility relative to the samples with jarosite present.

#### *4.5 Factors Controlling Lung Bioaccessibility*

With the partial exception of arsenic in sample B, *in vitro* bioaccessibilities for all measured elemental species were lower in lung fluid than gastric fluid. Solubility

constants for most Fe(III) oxides are on the order of  $10^{-4}$  (Schwertmann & Cornell, 2003); solubilities under circumneutral conditions are exceedingly low. Other metal oxides and metal carbonates also exhibit low solubility under these conditions. As a result, the mechanism of metal cation release from the tailings samples is most likely the rapid solvation of soluble salts such as sulfates followed by rapid hydrolysis and precipitation of amorphous metal oxides and metal carbonates, the most prevalent of which was ferrihydrite. Because the synthetic lung fluid is oxygenated, oxidative dissolution of pyrite was also found to play an important role in the release of metal(oids) *in vitro*.

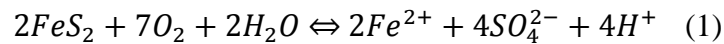
#### **4.5.1 Metal Cation Hydrolysis and Precipitation**

Fe(III) oxides are highly insoluble under oxic neutral conditions, and  $\text{Fe}^{3+}_{(\text{aq})}$  precipitates rapidly out of solution in the form of Fe(III) oxyhydroxides (particularly ferrihydrite) and oxyhydroxysulfates, as shown by the precipitation of these solid phases in the SLF-reacted samples from layers A-E. The larger initial rate of Fe release from samples A, C, D and E suggests that a large portion of the Fe in these samples is in the form of soluble sulfate salts. This larger Fe release results in a substantially lower fractional As bioaccessibility during lung fluid reaction, as  $\text{HAsO}_4^{2-}_{(\text{aq})}$  is readily adsorbed or incorporated into the structure of precipitated ferrihydrite (Waychunas et al., 1993) and jarosite (Savage et al., 2005). However, Fe release from samples F and G showed the opposite trend: Fe was released gradually at substantially higher concentrations than observed for any other sample, and did not precipitate out of solution for the first 24 h. This suggests that most of the Fe released from these samples was in the form of  $\text{Fe}^{2+}_{(\text{aq})}$  resulting from oxidative dissolution of pyrite, as solutions comprising

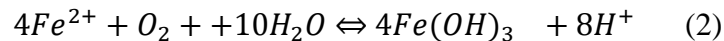
Fe(III) at the measured concentrations would be supersaturated in respect to ferrihydrite and other Fe(III) oxides. A majority of the  $Fe_{(aq)}$  in the other samples is most likely  $Fe^{2+}_{(aq)}$  as well, as a solution with these concentrations of  $Fe^{3+}_{(aq)}$  would be heavily supersaturated relative to ferrihydrite.

#### 4.5.2 Redox Processes

Because the synthetic lung fluid used in these experiments was oxygenated, oxidative processes have a substantive effect on trace element release into solution, especially for sulfide -rich samples. When exposed to  $O_2$  and water, metal sulfide particle surfaces undergo oxidative dissolution (Eqn. 1), acidifying the solution and releasing  $Fe^{2+}_{(aq)}$ ,  $SO_4^{2-}$  and trace elements from the sulfide fraction (including As and Pb).



Under the oxic, circumneutral conditions that exist in synthetic lung fluid,  $Fe^{2+}_{(aq)}$  is unstable and rapidly oxidized to  $Fe^{3+}_{(aq)}$ . Therefore, following oxidative sulfide dissolution, it is likely that the  $Fe^{2+}_{(aq)}$  in solution is further oxidized to  $Fe^{3+}_{(aq)}$  (Eqn. 2). Because the solubility of Fe(III) oxides is very low, this results in supersaturated conditions for ferrihydrite and precipitation is expected, which was observed in samples F and G, which showed concurrent decreases in aqueous Fe and As concentrations.



#### 4.5.3 Desorption Processes

Although ferrihydrite dissolution was observed in lung fluid, desorption and ligand exchange may have played a major role in controlling the release of trace elements (especially  $\text{HAsO}_4^{2-}(\text{aq})$ ) into solution. Some of the inorganic and organic ligands in synthetic lung fluid (i.e.  $\text{HPO}_4^{2-}$ , tartrate & citrate) have high affinities for ferrihydrite's surface and can compete with  $\text{HAsO}_4^{2-}(\text{aq})$  for binding sites (Jain & Loeppert, 2000; Grafe et al., 2002), allowing ligand exchange and release of  $\text{HAsO}_4^{2-}(\text{aq})$  into solution. However, the relative contributions of dissolution and desorption processes to trace element release cannot be quantified with the available data.

#### *4.5.4 Effect of Ligand Complexation on Mineral Dissolution and Precipitation*

During the reactions of samples A-D with lung fluid, Fe XAS fits indicated large-scale redistribution of Fe from ferrihydrite and schwertmannite to jarosite. Although these solutions were supersaturated relative to jarosite, this observation was surprising because this transformation requires dissolution of ferrihydrite prior to jarosite precipitation, and the solubility of ferrihydrite at neutral pH is essentially zero. However, anionic complexing agents in solution such as  $\text{Cl}^-$  (Schwertmann & Cornell, 2003) and citrate (Schwertmann, 1991) are capable of accelerating ferrihydrite dissolution by forming surface complexes with Fe(III) octahedral centers, making these mineralogical changes plausible. Ligand complexation of  $\text{Fe}^{3+}(\text{aq})$  also increases the solubility of these minerals. In addition, jarosite is highly insoluble under circumneutral conditions, and the presence of jarosite in these samples allows the observed precipitation of jarosite in the lung fluid reactions.

#### 4.5.5 Schwertmannite Transformation

Schwertmannite, a short-range order Fe(III) oxyhydroxysulfate, is an important component of sample C (Table 3) and possibly other samples due to its stability under acidic conditions with high levels of  $\text{SO}_4^{2-}$ . In previous studies exposing schwertmannite to circumneutral conditions similar to the synthetic lung fluid used in these experiments (Schroth & Parnell, 2005; Davidson et al., 2008), the mineral was found to transform to goethite with ferrihydrite as an intermediate. This transformation occurs due to removal of  $\text{SO}_4^{2-}$  from the schwertmannite structure, a process indicated in this experiment by changes in Fe and S speciation. Schroth and Parnell (2005) and Acero et al. (2006) observed that trace elements such as As and Pb were released from schwertmannite during its transformation to goethite *in situ*, but it is unknown if this release occurred during its initial transformation to the ferrihydrite intermediate. If schwertmannite is present in sample B, this may account for the unexpectedly high As release into SLF.

## 6. CONCLUSION

Although the generation of acid mine drainage and the mineralogical changes associated with oxidative weathering of mine wastes are well-characterized, the behavior of initially deposited and secondary tailings particles upon introduction into biological systems has not been thoroughly investigated. This experiment investigated the kinetics of contaminant As and Pb release in synthetic biofluids from samples collected across a gossan oxidative weathering profile formed over the 50 years since the tailings were first applied at the site. We found that oxidative weathering decreases the trace element bioaccessibility by oxidizing Fe, the dominant metal species at the site, and thereby

inducing the formation of secondary precipitates such as jarosite capable of sequestering As and Pb, the dominant trace element species found in the tailings pile. By revealing how contaminant bioaccessibility is controlled in this environment, the results of this experiment should inform measures to limit contaminant bioaccessibility at IKMHSS and similar tailings sites.

## Supplementary Information:

### *1. Specifications of PM<sub>10</sub> Generator*

A rectangular plexiglass window was added to the exterior of the rotating drum to facilitate addition and removal of bulk tailings material and to allow cleaning of the drum's interior when the fractionation process was complete. A 3.2 cm PVC pipe was also threaded through the center of the drum through orifices that are sealed with insulating foam, Vaseline, and duct tape to allow the PVC pipe to remain fixed while the drum rotated. Air flow through the drum was provided by a compressor and then flowed through a coalescing filter, a pressure regulator, a flow regulator and an orifice flow meter, all of which were used to keep the pressure gradient at a constant 5 psi. After the PVC pipe entered the dust generation chamber, a closed ball valve inserted in the center of the pipe forced air to exit the PVC pipe through holes drilled in the bottom.

After the air exited the generation chamber, it flowed tangentially into a cyclone separator (Model URG-2000-30EA, URG Corp., Chapel Hill, NC) used for dust fractionation with a design cut-point parameter of 10  $\mu\text{m}$  at a flow rate of 28.3 LPM. The fine particles were transported out of the cyclone separator and into the collection chamber, which was constructed from a polyethylene Ziploc freezer bag with a 20cm x

20cm window covered by an orange felt filter capable of entraining suspended particles flowing into the collection chamber. The window was designed to be as large as possible to prevent dust particles from clogging the felt filter, which had been found to cause pressure buildup and leakage in the dust generator in earlier tests of the apparatus. After the dust fractions were collected, they were removed and stored at room temperature.

2. *Composition of Synthetic Lung Fluid*

<b>Formula</b>	<b>Mass Added to 1L H<sub>2</sub>O (g)</b>	<b>Conc. (mmol/L)</b>
<b>MgCl<sub>2</sub>*6H<sub>2</sub>O</b>	0.2188	0.2269
<b>NaCl</b>	6.4148	109.8
<b>CaCl<sub>2</sub>*2H<sub>2</sub>O</b>	0.2568	1.747
<b>Na<sub>2</sub>SO<sub>4</sub></b>	0.0787	0.5541
<b>Na<sub>2</sub>HPO<sub>4</sub></b>	0.1497	1.055
<b>NaHCO<sub>3</sub></b>	2.7056	32.21
<b>Sodium Tartrate Dihydrate</b>	0.1810	0.7867
<b>Sodium Citrate Dihydrate</b>	0.1539	0.5233
<b>Sodium Lactate</b>	0.1736	0.9295
<b>Sodium Pyruvate</b>	0.1774	1.612
<b>Glycine</b>	0.1183	1.576

## 7. REFERENCES

- Abernathy, C. O., Liu, Y. P., Longfellow, D., Aposhian, H. V., Beck, B., Fowler, B., Goyer, R., Menzer, R., Rossman, T., Thompson, C. & Waalkes, M. (1999). Arsenic: Health effects, mechanisms of actions, and research issues. *Environmental Health Perspectives*, 107, 593-597.
- Acerro, P., Ayora, C., Torrento, C., & Nieto, J. M. (2006). The behavior of trace elements during schwertmannite precipitation and subsequent transformation into goethite and jarosite. *Geochimica Et Cosmochimica Acta*, 70, 4130-4139.
- Agency for Toxic Substances and Disease Registry, 2016. Priority List of Hazardous Substances. Available at <http://www.atsdr.cdc.gov/spl/>. Accessed April 20, 2016.
- Ahsan, H., Chen, Y., Parvez, F., Argos, M., Hussain, A. I., Momotaj, H., Levy, D., van Geen, A., Howe, G., Graziano, J. (2006). Health effects of arsenic longitudinal study (HEALS): Description of a multidisciplinary epidemiologic investigation. *Journal of Exposure Science and Environmental Epidemiology*, 16, 191-205.
- Barney, G. O. (1980). *The global 2000 report to the President of the United States*. New York: Pergamon Press.
- Basu, A., & Schreiber, M. E. (2013). Arsenic release from arsenopyrite weathering: Insights from sequential extraction and microscopic studies. *Journal of Hazardous Materials*, 262, 896-904.
- Beak, D. B., Basta, N. T., Scheckel, K. G., & Traina, S. J. (2006). Bioaccessibility of arsenic (V) bound to ferrihydrite using a simulated gastrointestinal system. *Environmental Science and Technology*, 40, 1364-1370.
- Beckmann, W. (2013). *Crystallization: Basic concepts and industrial applications*. Weinheim, Germany: Wiley-VCH.
- Bethke, C. M. (2008). *Geochemical and biogeochemical reaction modeling* (2nd Ed. ed.). Cambridge, UK: Cambridge University Press.
- Bigham, J. M., & Nordstrom, D. K. (2000). Iron and aluminum hydroxysulfates from acid sulfate waters. *Reviews in Mineralogy and Geochemistry*, 40, 351-403.
- Bigham, J. M., Schwertmann, U., Traina, S. J., Winland, R. L., & Wolf, M. (1996). Schwertmannite and the chemical modelling of iron in acid sulfate waters. *Geochimica Et Cosmochimica Acta*, 60, 2111-2121.
- Blowes, D. W., Ptacek, C. J., Jambor, J. L., & Weisener, C. G. (2003). The geochemistry of acid mine drainage. *Treatise on Geochemistry*, 9, 612.

- Blowes, D. W., & Jambor, J. L. (1990). The pore-water geochemistry and the mineralogy of the vadose zone of sulfide tailings, waite amuley, quebec, canada. *Applied Geochemistry*, 5, 327-346.
- Boisa, N., Elom, N., Dean, J. R., Deary, M. E., Bird, G., & Entwistle, J. E. (2014). Development and application of an inhalation bioaccessibility method (IBM) for lead in the PM<sub>10</sub> size fraction of soil. *Environment International*, 70, 132-142.
- Boulet, M. P., & Larocque, A. C. L. (1998). A comparative mineralogical and geochemical study of sulfide mine tailings at two sites in new mexico, USA. *Environmental Geology*, 33(2), 130-142.
- Bressler, J. P., & Goldstein, G. W. (1991). Mechanisms of lead neurotoxicity. *Biochemical Pharmacology*, 41, 479-484.
- Bunker, G. (2010). *Introduction to EXAFS: A practical guide to X-ray absorption fine structure spectroscopy*. Cambridge, UK: Cambridge University Press.
- Burton, E. D., Bush, R. T., Johnston, S. G., Watling, K. M., Hocking, R. K., Sullivan, L. A., & Parker, G. K. (2009). Sorption of as (V) and as (III) to schwertmannite. *Environmental Science and Technology*, 43, 9202-9207.
- Chao, T. T., & Zhou, L. (1982). Extraction techniques for selective dissolution of amorphous iron oxides from soils and sediments. *Soil Science Society of America Journal*, 47(2), 225-232.
- Catalano, J. G., Zhang, Z., Park, C., Fenter, P., & Bedzyk, M. J. (2007). Bridging arsenate surface complexes on the hematite (012) surface. *Geochimica et Cosmochimica Acta*, 71(8), 1883-1897.
- Cismasu, A. C., Michel, F. M., Tcaciuc, A. P., Tyliczszak, T., & Brown, G. E. (2011). Composition and structural aspects of naturally occurring ferrihydrite. *Comptes Rendus Geoscience*, 343(2-3), 210-218.
- Concas, A., Arda, C., Cristini, A., Zuddas, P., & Cao, G. (2006). Mobility of heavy metals from tailings to stream waters in a mining activity contaminated site. *Chemosphere*, 63, 244-253.
- Cornell, R. M., & Schwertmann, U. (2000). *Iron oxides in the laboratory: Preparation and characterization*. Weinheim, Germany: Wiley-VCH.
- Cornell, R. M., & Schwertmann, U. (2003). *The iron oxides: Structure, properties, reactions, occurrences and uses* (2nd Ed. ed.). Weinheim, Germany: Wiley-VCH. doi:10.1002/3527602097
- Craw, D., & Bowell, R. J. (2014). The characterization of arsenic in mine waste. *Reviews in Mineralogy and Geochemistry*, 79, 473-505.

- Creasey, S. C. (1952). Geology of the iron king mine, yavapai county, arizona. *Economic Geology*, 47, 24-56.
- Csavina, J., Field, J., Taylor, M. P., Gao, S., Landazuri, A., Betterton, E. A., & Saez, E. A. (2012). A review on the importance of metals and metalloids in atmospheric dust and aerosol from mining operations. *Science of the Total Environment*, 433, 58-73.
- Davidson, L. E., Shaw, S., & Benning, L. G. (2008). The kinetics and mechanisms of schwertmannite transformation to goethite and hematite under alkaline conditions. *American Mineralogist*, 93, 1326-1337.
- Davis, J. A., & Kent, D. B. (1990). Surface complexation modeling in aqueous geochemistry. *Reviews in Mineralogy and Geochemistry*, 23(1), 177-260.
- Dixit, S., & Hering, J. G. (2003). Comparison of arsenic (V) and arsenic (III) sorption onto iron oxide minerals: Implications for arsenic mobility. *Environmental Science & Technology*, 37, 4182-4189.
- Dold, B., & Fontboté, L. (2001). Element cycling and secondary mineralogy in porphyry copper tailings as a function of climate, primary mineralogy, and mineral processing. *Journal of Geochemical Exploration*, 74(1), 3-55.
- Driscoll, R., & Leinz, R. (2005). *Methods for synthesis of some jarosites* (No. 5-D1).
- Dudka, S., & Adriano, D. C. (1997). Environmental impacts of metal ore mining and processing: a review. *Journal of Environmental Quality*, 26(3), 590-602.
- Dutrizac, J. E., Jambor, J.L. (2000). Jarosites and their application in hydrometallurgy. In C. N. Alpers, J. L. Jambor & D. K. Nordstrom (Eds.), *Sulfate minerals: Crystallography, geochemistry, and environmental significance, reviews in mineralogy and geochemistry, vol. 40*. (pp. 405-453).
- Fendorf, S., Eick, M. J., Grossl, P., & Sparks, D. L. (1997). Arsenate and chromate retention mechanisms on goethite. 1. Surface structure. *Environmental Science & Technology*, 31(2), 315-320.
- Forray, F. L., Smith, A. M., Drouet, C., Navrotsky, A., Wright, K., Hudson-Edwards, K. A., & Dubbin, W. E. (2010). Synthesis, characterization and thermochemistry of a Pb-jarosite. *Geochimica et Cosmochimica Acta*, 74(1), 215-224.
- Foster, A. L., Brown, G. E., Tingle, T. N., & Parks, G. A. (1998). Quantitative arsenic speciation in mine tailings using X-ray absorption spectroscopy. *American Mineralogist*, 83, 553-568.

- Fuller, C. C., Davis, J. A., & Waychunas, G. A. (1993). Surface chemistry of ferrihydrite: Part 2. kinetics of arsenate adsorption and coprecipitation. *Geochimica Et Cosmochimica Acta*, 57, 2271-2282.
- Galley, A. G., Hannington, M. D., & Jonassen, I. R. (2007). Volcanogenic massive sulphide deposits. In W. D. Goodfellow (Ed.), *Mineral deposits of Canada: A synthesis of major deposit-types, district metallogeny, the evolution of geological provinces, and exploration methods*. (pp. 141-161). St. John's, Newfoundland: Geological Association of Canada, Mineral Deposits Division.
- Grafe, M., Eick, M. J., Grossl, P. R., & Saunders, A. M. (2002). Adsorption of arsenate and arsenite on ferrihydrite in the presence and absence of dissolved organic carbon. *Journal of Environmental Quality*, 31, 1115-1123.
- Hayes, S. M., White, S. A., Thompson, T. L., Maier, R. M., & Chorover, J. (2009). Changes in lead and zinc lability during weathering-induced acidification of desert mine tailings: Coupling chemical and micro-scale analyses. *Applied Geochemistry*, 24, 2234-2245.
- Hayes, S. M., Webb, S. M., Bargar, J. R., O'Day, P. A., Maier, R. M., & Chorover, J. (2012). Geochemical weathering increases lead bioaccessibility in semi-arid mine tailings. *Environmental Science and Technology*, 46, 5834-5841.
- Hayes, S. M., Root, R. A., Perdrial, N., Maier, R. M., & Chorover, J. (2014). Surficial weathering of iron sulfide mine tailings under semi-arid climate. *Geochimica Et Cosmochimica Acta*, 141, 240-257.
- Hudson-Edwards, K. A., Schell, C., & Macklin, M. G. (1999). Mineralogy and geochemistry of alluvium contaminated by metal mining in the Rio Tinto area, southwest Spain. *Applied Geochemistry*, 14(8), 1015-1030.
- Jain, A., & Loeppert, R. H. (2000). Effect of competing anions on the adsorption of arsenate and arsenite by ferrihydrite. *Journal of Environmental Quality*, 29, 1422-1430.
- Jambor, J. L., Nordstrom, D. K., & Alpers, C. N. (2000). Metal sulfate salts from sulfide mineral oxidation. In P. H. Ribbe (Ed.), *Sulfate minerals- crystallography, geochemistry, and environmental significance* (pp. 303-350). Washington, D.C.: Mineralogical Society of America.
- Johnson, D. B. (2003). Chemical and microbiological characteristics of mineral spoils and drainage waters at abandoned coal and metal mines. *Water, Air and Soil Pollution*, 3, 47-66.
- Johnson, D. B., & Hallberg, K. B. (2005). Acid mine drainage remediation options: A review. *Science of the Total Environment*, 338(1), 3-14.

- Kashkay, C. M., Borovskaya, Y. B., & Badazade, M. A. (1975). Determination of  $\Delta G^{\circ}_f$  of synthetic jarosite and its sulfate analogues. *Geochemistry International*, 12(3), 115-121.
- Kelley, M. E., Grauning, S. E., Schoof, R. A., & Ruby, M. V. (2002). *Assessing oral bioavailability of metals in soil*. Columbus, OH: Battelle Press.
- Kim, K. J. (2008). Characteristics of synchrotron radiation. In *Physics of Particle Accelerators* (Vol. 184, No. 1, pp. 565-632). AIP Publishing.
- Kim, C. S., Chi, C., Miller, S. R., Rosales, R. A., Sugihara, E. S., Akau, J., Rytuba, J.J. & Webb, S. M. (2013). (Micro) spectroscopic analyses of particle size distributions in mine wastes: Implications for water contamination and human exposure. *Environmental Science and Technology*, 26, 484-495.
- Lengke, M. F., Sanpawanitchakit, C., & Tempel, R. N. (2009). The oxidation and dissolution of arsenic-bearing sulfides. *The Canadian Mineralogist*, 47, 593-613.
- Konigsberger, D., & Prins, R. (1988). *X-ray Absorption: Principles, Techniques and Applications of EXAFS and XANES*. New York: Wiley.
- Lengke, M. F., Sanpawanitchakit, C., & Tempel, R. N. (2009). The oxidation and dissolution of arsenic-bearing sulfides. *The Canadian Mineralogist*, 47, 593-613.
- Lidsky, T. I., & Schneider, J. S. (2003). Lead neurotoxicity in children: Basic mechanisms and clinical correlates. *Brain*, 126, 5-19.
- Lottermoser, B. G. (2011). Recycling, reuse and rehabilitation of mine wastes. *Elements*, 7, 405-410.
- Mendez, M. O., & Maier, R. M. (2008). Phytoremediation of mine tailings in temperate and arid environments. *Reviews in Environmental Science and Biotechnology*, 7, 47-59.
- Menka, N., Root, R. A., & Chorover, J. (2014). Bioaccessibility, release kinetics, and molecular speciation of arsenic and lead in geo-dusts from the iron king mine federal superfund site in dewey-humboldt, arizona. *Reviews on Environmental Health*, 9(1-2), 23-27.
- Meza-Figueroa, D., Maier, R. M., de la O-Villanueva, M., Gomez-Alvarez, A., Moreno-Zazueta, A., Rivera, J., Campillo, A., Grandlic, C.J., Anaya, R., Palafox-Reyes, J. (2009). The impact of unconfined mine tailings in residential areas from a mining town in a semi-arid environment: Nacozari, Sonora, Mexico. *Chemosphere*, 77(1), 140-147.

- Miller, D. D., Schrickler, B. R., Rasmussen, R. R., & Van Campen, D. (1981). An *in vitro* method for estimation of iron availability from meals. *The American Journal of Clinical Nutrition*, 34(10), 2248-2256.
- Misra, K. G. (2012). *Introduction to geochemistry: Principles and applications* (1st Ed. ed.). Hoboken, NJ: Wiley-Blackwell.
- Moldovan, B. J., Jiang, D. T., & Hendry, M. J. (2003). Mineralogical characterization of arsenic in uranium mine tailings precipitated from iron-rich hydrometallurgical solutions. *Environmental Science & Technology*, 37(5), 873-879.
- Morin, G., Ostergren, J. D., Juillot, F., Ildefonse, P., Calas, G., & Brown, G. E. (1999). XAFS determination of the chemical form of lead in smelter-contaminated soils and mine tailings: Importance of adsorption processes. *American Mineralogist*, 84, 420-434.
- Morse, J. W., & Casey, W. H. (1988). Ostwald processes and mineral paragenesis in sediments. *American Journal of Science*, 288, 537-560.
- Moss, O. R. (1979). Simulants of lung interstitial fluid. *Health Physics*, 36(3), 447-448.
- Navarro, A., Collado, D., Carbonell, M., & Sanchez, J. A. (2004). Impact of mining activities on soils in a semi-arid environment: Sierra almagrera district, SE Spain. *Environmental Geochemistry and Health*, 26, 383-393.
- Nieto, J. M., Capitan, M. A., Saez, R., & Almodovar, G. R. (2003). Beudantite: A natural sink for As and Pb in sulphide oxidation processes. *Applied Earth Science*, 112(3), 293-296.
- O'Day, P. A., Rivera, N., Root, R., & Carroll, S. A. (2004a). X-ray absorption spectroscopic study of Fe reference compounds for the analysis of natural sediments. *American Mineralogist*, 89(4), 572-585.
- O'Day, P. A., Vlassopoulos, D., Root, R., & Rivera, N. (2004b). The influence of sulfur and iron on dissolved arsenic concentrations in the shallow subsurface under changing redox conditions. *Proceedings of the National Academy of Sciences of the United States of America*, 101(38), 13703-13708.
- O'Day, P. A. (2006). Chemistry and mineralogy of arsenic. *Elements*, 2(2), 77-83.
- Oomen, A. G., Hack, A., Minekus, M., Zeijdner, E., Cornelis, C., Schoeters, G., Verstraete, W., Van de Wiele, T., Wragg, J., Rompelberg, C.J., Sips, A.J. & Van Wijnen, J.H. (2002). Comparison of five *in vitro* digestion models to study the bioaccessibility of soil contaminants. *Environmental Science & Technology*, 36(15), 3326-3334.

- Ostergren, J. D., Brown, G. E., Parks, G. E., & Tingle, T. N. (1999). Quantitative speciation of lead in selected mine tailings from leadville, CO. *Environmental Science and Technology*, 33, 1627-1636.
- Paige, C. R., Snodgrass, W. J., Nicholson, R. V., & Scharer, J. M. (1997). An arsenate effect on ferrihydrite dissolution kinetics under acidic oxic conditions. *Water Research*, 31(9), 2370-2382.
- Paktunc, D., & Dutrizac, J. E. (2003). Characterization of arsenate-for-sulfate substitution in synthetic jarosite using x-ray diffraction and x-ray absorption spectroscopy. *The Canadian Mineralogist*, 41, 905-919.
- Paktunc, D., Foster, A. L., Heald, S., & Laflamme, G. (2004). Speciation and characterization of arsenic in gold ores and cyanidation tailings using X-ray absorption spectroscopy. *Geochimica Et Cosmochimica Acta*, 68, 969-983.
- Ramirez-Andreotta, M. D., Brusseau, M. L., Beamer, P., & Maier, R. M. (2013). Home gardening near a mining site in an arsenic-endemic region of Arizona: Assessing arsenic exposure dose and risk via ingestion of home garden vegetables, soils, and water. *Science of the Total Environment*, 454-455, 373-382.
- Ravel, B., & Newville, M. (2005). ATHENA, ARTEMIS, HEPHAESTUS: Data analysis for X-ray absorption spectroscopy using IFEFFIT. *Journal of Synchrotron Radiation*, 12, 537-541.
- Raven, K. P., Jain, A., & Loeppert, R. H. (1998). Arsenite and arsenate adsorption on ferrihydrite: Kinetics, equilibrium, and adsorption envelopes. *Environmental Science and Technology*, 32, 344-349.
- Regenspurg, S., Brand, A., & Peiffer, S. (2004). Formation and stability of schwertmannite in acidic mining lakes. *Geochimica et Cosmochimica Acta*, 68(6), 1185-1197.
- Regenspurg, S., & Peiffer, S. (2005). Arsenate and chromate incorporation in schwertmannite. *Applied Geochemistry*, 20, 1226-1239.
- Rico, M., Benito, G., Salgueiro, A. R., Díez-Herrero, A., & Pereira, H. G. (2008). Reported tailings dam failures: a review of the European incidents in the worldwide context. *Journal of Hazardous Materials*, 152(2), 846-852.
- Rimstidt, D. R., Chermak, J. A., & Gagen, P. M. (1994). Rates of reaction of galena, sphalerite, chalcopyrite, and arsenopyrite with Fe(III) in acidic solutions. In C. N. Alpers, & D. W. Blowes (Eds.), *Environmental geochemistry of sulfide oxidation* (pp. 2-13). Washington, DC: American Chemical Society.

- Rodriguez, R. R., Basta, N. T., Casteel, S. W., & Pace, L. W. (1999). An *in vitro* gastrointestinal method to estimate bioavailable arsenic in contaminated soils and solid media. *Environmental Science and Technology*, 33, 642-649.
- Root, R. A., Hayes, S. M., Hammond, C. M., Maier, R. M., & Chorover, J. (2015). Toxic metal (loid) speciation during weathering of iron sulfide mine tailings under semi-arid climate. *Applied Geochemistry*, 62, 131-149.
- Ruby, M. V., Davis, A., Schoof, R., Eberle, S., & Sellstone, C. M. (1996). Estimation of lead and arsenic bioavailability using a physiologically based extraction test. *Environmental Science and Technology*, 30, 422-430.
- Ruby, M. V., Schoof, R., Brattin, W., Goldade, M., Post, G., Harnois, M., Mosby, D.E., Casteel, S.W., Berti, W., Carpenter, M., Edwards, D., Cragin, D., & Chappell, W. (1999). Advances in evaluating the oral bioavailability of inorganics in soil for use in human health risk assessment. *Environmental Science & Technology*, 33(21), 3697-3705.
- Savage, K. S., Bird, D. K., & O'Day, P. A. (2005). Arsenic speciation in synthetic jarosite. *Chemical Geology*, 215, 473-485.
- SBRC. (2001). *Standard operating procedure: in vitro method for determination of lead and arsenic bioavailability*. Unpublished manuscript.
- Scholze, H., & Conradt, R. (1987). An *in vitro* study of the chemical durability of siliceous fibers. *The Annals of Occupational Hygiene*, 31, 683-692.
- Schroth, A. W., & Parnell Jr., R. A. (2005). Trace metal retention through the schwertmannite to goethite transformation as observed in a field setting, alta mine, MT. *Applied Geochemistry*, 20, 907-917.
- Schwertmann, U. (1991). Solubility and dissolution of iron oxides. In Y. Chen, & Y. Hadar (Eds.), *Iron nutrition and interactions in plants*. (pp. 3-27). Dordrecht, Netherlands.: Kluwer Academic Publishers.
- Sherman D.M., Randall, S.R. (2003). Surface complexation of arsenic (V) to iron (III) hydroxides: Structural mechanism from ab initio molecular geometries and EXAFS spectroscopy. *Geochimica Et Cosmochimica Acta*, 67, 4223-4230.
- Sorokin, S. P., & Brain, J. D. (1975). Pathways of clearance in mouse lungs exposed to iron oxide aerosols. *The Anatomical Record*, 181(3), 581-625.
- Stopford, W., Turner, J., Cappellini, D., & Brock, T. (2003). Bioaccessibility testing of cobalt compounds. *Journal of Environmental Monitoring*, 5(4), 675-680.

- Stovern, M., Felix, O., Csavina, J., Rine, K. P., Russell, M. R., Jones, M. R., Saez, E. A. (2014). Simulation of windblown dust transport from a mine tailings impoundment using a computational fluid dynamics model. *Aeolian Research*, 14, 75-83.
- Stovern, M., Guzman, H., Rine, K. P., Felix, O., King, M., Ela, W. P., Betterton, E.A., Saez, A. E. (2016). Windblown dust deposition forecasting and spread of contamination around mine tailings. *Atmosphere*, 7(2), 16.
- Takaya, M., Shinohara, Y., Serita, F., Ono-Ogasawara, M., Otaki, N., Toya, T., Takata, T., Yoshida, K. & Kohyama, N. (2006). Dissolution of functional materials and rare earth oxides into pseudo alveolar fluid. *Industrial Health*, 44, 639-644.
- Taunton, A. E., Gunter, M. E., Druschel, G. K., & Wood, S. A. (2010). Geochemistry in the lung: Reaction-path modeling and experimental examination of rock-forming minerals under physiologic conditions. *American Mineralogist*, 95(11), 1624.
- Wang, H., Bigham, J. M., & Tuovinen, O. H. (2006). Formation of schwertmannite and its transformation to jarosite in the presence of acidophilic iron-oxidizing microorganisms. *Materials Science and Engineering: C*, 26(4), 588-592.
- Waychunas, G. A., Rea, R. A., Fuller, C. C., & Davis, J. A. (1993). Surface chemistry of ferrihydrite: Part 1. EXAFS studies of the geometry of coprecipitated and adsorbed arsenate. *Geochimica Et Cosmochimica Acta*, 57, 2251-2269.
- Webb, S. M. (2005). SixPACK: A graphical user interface for XAS analysis using IFEFFIT. *Physica Scripta*, T1115, 1011-1014.
- Webster, J. G., Swedlund, P. J., & Webster, K. S. (1998). Trace metal adsorption onto an acid mine drainage iron (III) oxyhydroxysulfate. *Environmental Science and Technology*, 32, 1361-1368.
- Wills, B. A. (2006). *Wills' mineral processing technology: An introduction to the practical aspects of ore treatment and mineral recovery*. (7th Ed.). Oxford, UK: Butterworth-Heinemann.
- Winick, H., Brown, G., Halbach, K., & Harris, J. (1981). Wiggler and undulator magnets. *Physics Today*, 34(5), 50-63.
- Wray, D. S. (1998). The impact of unconfined mine tailings and anthropogenic pollution on a semi-arid environment—an initial study of the Rodalquilar mining district, south east Spain. *Environmental Geochemistry and Health*, 20(1), 29-38.
- Yang, X., Zhu, M., Kang, F., Cao, S., Chen, R., Liu, H., & Wei, Y. (2015). Formation mechanism of a series of trigonal antiprismatic jarosite-type compounds. *Journal of Crystal Growth*, 429, 49-55.

